# UC Berkeley
## UC Berkeley Previously Published Works

**Title**

The Counterintuitive Relationship between Orbital Energy, Orbital Overlap, and Bond Covalency in CeF62- and CeCl62.

**Permalink**

https://escholarship.org/uc/item/3vn3k818

**Journal**

Journal of the American Chemical Society, 146(37)

**Authors**

Branson, Jacob
Smith, Patrick
Sergentu, Dumitru-Claudiu
et al.

**Publication Date**

2024-09-18

**DOI**

10.1021/jacs.4c07459

Peer reviewed

Open Access

This article is licensed under CC-BY-NC-ND 4.0

Article

# The Counterintuitive Relationship between Orbital Energy, Orbital Overlap, and Bond Covalency in $CeF_6^{2-}$ and $CeCl_6^{2-}$

Jacob A. Branson, Patrick W. Smith, Dumitru-Claudiu Sergentu, Dominic R. Russo, Himanshu Gupta, Corwin H. Booth, John Arnold, Eric J. Schelter, Jochen Autschbach,* and Stefan G. Minasian*

Read Online

ACCESS | Metrics & More | Article Recommendations | Supporting Information

**ABSTRACT:** The 4f orbitals of Ce(IV) have shown appreciably enhanced covalent mixing with ligand orbitals relative to those of Ce(III). Here, X-ray spectroscopy, magnetic susceptibility measurements, and theoretical methods are used to investigate 4f covalency in $CeF_6^{2-}$ and $CeCl_6^{2-}$. These techniques show covalent mixing between Ce 4f and F 2p orbitals to be about 25% less than mixing between Ce 4f and Cl 3p orbitals, placing $CeF_6^{2-}$ among the most ionic Ce(IV) compounds to-date. However, ligand field analysis using the experimental data shows significantly higher 4f orbital overlap with the F 2p orbitals compared to the Cl 3p. This result is counterintuitive since the Ce−F bonds display less 4f covalency despite their higher orbital overlap, and greater overlap is traditionally associated with enhanced bond covalency. The weaker covalency is attributed to the large energy gap between Ce 4f and F 2p orbitals strongly countering the higher orbital overlap. These results highlight that only a concerted consideration of both atomic orbital overlap and energy matching in f-element systems leads to an accurate picture of their bonding.
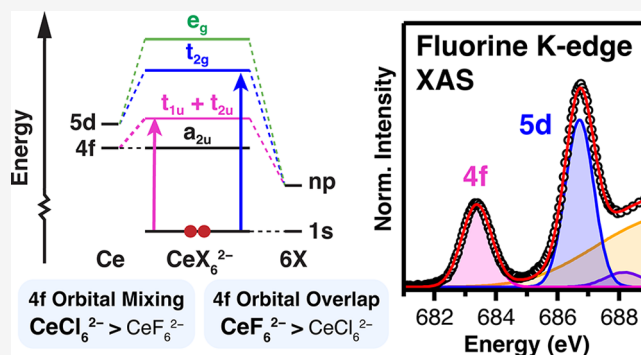
## INTRODUCTION

Cerium holds a unique position among the other lanthanide elements because it can access the tetravalent $(4f^0)$ oxidation state in a wide range of chemical environments. In its trivalent state, spectroscopic and computational techniques have shown that the Ce 4f orbitals are core-like and only weakly involved in covalent bonding.[1−4] Conversely, 4f covalency is frequently invoked in descriptions of chemical bonding for tetravalent Ce compounds.[5−10] This versatility in accessible redox states and modes of chemical bonding has enabled a wide range of reactivity in Ce compounds including C−C bond activation, photocatalysis, and oxygen transfer.[10−20] For Ce intermetallic compounds, strong electron correlations can have a significant impact on electronic structure and lead to properties such as heavy fermion behavior, Kondo magnetism, superconductivity, and intermediate Ce valency.[21−25] Because of these unique electronic properties, Ce compounds have found technological applications in fields from catalysis and petroleum refinement to national security.[26] Consequently, it is of increasing importance to develop improved models of Ce electronic structure that can provide a means to control its physical properties rationally.

A state-of-the-art approach to probing bond covalency applies X-ray spectroscopic techniques in tandem with electronic structure calculations. Cerium L₃-edge $(2p_{3/2} \rightarrow 5d_{5/2})$ X-ray absorption spectroscopy (XAS) has been

established as a versatile tool for probing the amount of 4f-electron density residing on a Ce(IV) ion.[27−31] The L₃-edge spectra exhibit features corresponding to a Ce(III)/Ce(IV) configuration interaction (CI) in the ground state and/or the probed core-excited states. Sergentu et al. have shown that both types of states have to be considered to evaluate the ground-state electronic structure correctly.[32] From the relative intensities of the CI features, the effective number of Ce 4f electrons is determined as a value called $n_f$. In addition to this metal-centered technique, measuring X-ray absorption spectra at the K-edge for ligand donor atoms, a technique known as ligand K-edge XAS, provides complementary insight into the metal−ligand covalency.[33−35] Ligand K-edge XAS transitions occur from 1s orbitals localized on the ligand into molecular orbitals (MOs) formed by mixing of valence ligand np atomic orbitals (AOs) with metal AOs.[36,37] This mixing is typically interpreted in terms of covalent bonding. The intensity of a pre-edge transition can be used to determine the amount of ligand p-orbital character in the acceptor MO, $\lambda^2$. Specifically,

$\lambda^2$ represents the population of a ligand AO in the MO and is related to $t'$, the mixing coefficient, corresponding to the weight of the ligand AO in the MO. The value $\lambda^2$ includes all the electron density associated with the ligand ($t'^2$) and half that in the region of metal−ligand orbital overlap ($t'S_{ML}$). From perturbational MO theory, larger values of $\lambda^2$ (and $t'^2$) can be achieved both by increasing the amount of orbital overlap ($S_{ML} = \int \varphi_M^* \varphi_L \, dV$) and also by decreasing the energy difference between the AOs.[38−41] It is important to note that $t'^2$ alone cannot be evaluated with ligand K-edge XAS, as this value alone is not associated with total ligand electron density.

In the present study, fluorine K-edge XAS is used to evaluate orbital mixing and overlap in $CeF_6^{2-}$. We chose $CeF_6^{2-}$ for comparison to the previously studied $CeCl_6^{2-}$. Since the ligand orbital energies of these complexes can be associated with their known ionization potentials, the electronic structures can be evaluated confidently within a ligand field model. By comparing these isostructural species with analogous techniques, rigorous comparisons of bond covalency, bond stabilization, and orbital overlap can be made. Results from ligand K-edge XAS are corroborated by Ce $L_3$-edge and $M_{4,5}$-edge XAS, SQUID magnetometry, spectral simulations, and ground-state electronic structure calculations. We adopted this breadth of methodologies to form a very precise data set and in order to calibrate these measurements of covalency to one another. Together, these techniques reveal $CeF_6^{2-}$ as among the (if not *the*) most ionic Ce(IV) compounds. However, overlap analysis from the ligand K-edge XAS spectra of this $CeF_6^{2-}$ compared to the reported $CeCl_6^{2-}$ finds significantly greater 4f-ligand AO overlap in the Ce−F bond compared to the Ce−Cl bond, despite the less covalent nature of the Ce−F bond.

## RESULTS

**Synthesis and Initial Characterization.** For this spectroscopic study, well-isolated $CeF_6^{2-}$ units with non-coordinating countercations are desirable to ensure that the Ce−F bonds were probed directly. Though $(Et_4N)_2CeF_6\cdot6H_2O$ has been reported,[42] the presence of water molecules could perturb with the Ce−F interactions via H-bonding. Therefore, a new anhydrous $CeF_6^{2-}$ salt with $Ph_4P^+$ countercations was prepared as a colorless crystalline solid in 79.5% yield from $(Et_4N)_2CeF_6\cdot6H_2O$ and two equivalents of $Ph_4PCl$. X-ray quality crystals for a single crystal X-ray diffraction study were grown by vapor diffusion of diethyl ether into an acetonitrile (MeCN) solution (Figure 1). The structure of $(Ph_4P)_2CeF_6$ has three unique Ce−F distances at 2.1599(14),
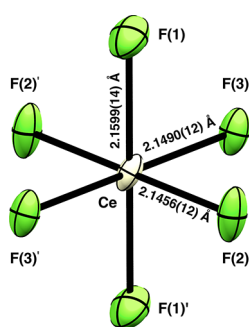


**Figure 1.** Crystal structure of $(Ph_4P)_2CeF_6$ (50% probability ellipsoids). $Ph_4P^+$ cations and co-crystallized MeCN are omitted for clarity.

2.1456(12) and 2.1490(12) Å. The average Ce−F distance in $(Ph_4P)_2CeF_6$ is 2.152(6) Å, which is similar to the average Ce−F distance of 2.148(10) Å reported for $(Et_4N)_2CeF_6\cdot6H_2O$.[42]

The UV−vis spectrum of $(Ph_4P)_2CeF_6$ in MeCN (Figure S3) shows multiple features resulting from coincident transitions associated with the $CeF_6^{2-}$ anion and $Ph_4P^+$ cations. However, the inflection point of the intense UV absorption band at 5.1 eV can be regarded as the lower bound of the LMCT energy, which agrees with the HOMO−LUMO gap determined from ground state electronic structure calculations, 5.99 eV (see Supporting Information). Vibrational spectroscopy shows an IR-active peak at 438.7 cm$^{-1}$ (Figure S4) and a Raman-active peak at 528 cm$^{-1}$ (Figure S5), which are assigned to the $CeF_6^{2-}$ octahedron. Previous studies on $HfF_6^{2-}$ and $HfCl_6^{2-}$ showed that the $HfF_6^{2-}$ vibrations are observed at higher energies relative to the $HfCl_6^{2-}$ vibrations owing to the higher mass of Cl.[43−45] Hence, by comparison to vibrational data published for $CeCl_6^{2-}$ where $\nu_1$ and $\nu_3$ modes were identified at 295 and 268 cm$^{-1}$,[46] the peaks at 528 and 438.7 cm$^{-1}$ in the vibrational spectra of $CeF_6^{2-}$ were assigned to $\nu_1$ and $\nu_3$ modes, respectively. A solution $^{19}$F NMR spectroscopy experiment on $(Ph_4P)_2CeF_6$ recorded in $CD_3CN$ exhibited a peak at 180.7 ppm (externally referenced against $CFCl_3$). Cyclic voltammetry (CV) of $(Ph_4P)_2CeF_6$ in MeCN showed no reversible redox features (Figure S6), suggesting that it was redox inactive within the electrochemical window of MeCN.

Comparison of the UV−vis and CV data reported here for $CeF_6^{2-}$ versus those for $CeCl_6^{2-}$ provides an initial evaluation of the electronic structure of these complexes. For $CeCl_6^{2-}$, the lowest energy LMCT from UV−vis is at 3.3 eV[2] and a reversible $CeCl_6^{2-}/CeCl_6^{3-}$ redox couple is observed at $E_{1/2} = -0.03$ V[13] versus Fc/Fc$^+$ (originally reported as the $CeCl_6^{3-}/CeCl_6^{2-}$ couple). Compared to the >5.1 eV LMCT and unobservable redox couple for $CeF_6^{2-}$, these data reveal a significantly higher energy separation between the HOMO and LUMO in $CeF_6^{2-}$ vs $CeCl_6^{2-}$. However, this information alone is not sufficient for evaluating bond covalency.

**SQUID Magnetometry.** Magnetic susceptibility data were collected from 3 to 400 K for $(Ph_4P)_2CeF_6$ and $(Et_4N)_2CeCl_6$ (Figure 2, left). The samples were contained in quartz tubes for measurement as previously described.[47−50] Diamagnetic corrections were applied for the quartz wool using Pascal's constants,[51] and a correction for ferromagnetic impurities was also applied as previously described.[52] Due to the small magnetic moments of these compounds, the magnetometry data were collected in triplicate to ensure high data quality. The $\chi$ vs $T$ data are fit to the Curie−Weiss Law to determine the Curie constant ($C$), the Curie−Weiss temperature ($\Theta$), and the temperature-independent paramagnetism (TIP) ($\chi_0$).

$$\chi = \frac{C}{T - \Theta} + \chi_0 \tag{1}$$

For $(Ph_4P)_2CeF_6$, the fit values are −4.3(2) K for $\Theta$, 2.2(3) × 10$^{-3}$ emu K mol$^{-1}$ for $C$, and 0.81(4) × 10$^{-4}$ emu mol$^{-1}$ for $\chi_0$. For $(Et_4N)_2CeCl_6$, the fit values are −1.5(1) K for $\Theta$, 1.1(1) × 10$^{-3}$ emu K mol$^{-1}$ for $C$, and 1.6(2) × 10$^{-4}$ emu mol$^{-1}$ for $\chi_0$. A plot of $\chi T$ vs $T$ (Figure 2, right) shows this difference visually, where $\Theta$ is set to zero and the slope of the line is equal to $\chi_0$. The nonzero values of $C$ indicate the presence of trace paramagnetic impurities in these samples. While the identity of these impurities is unknown, the
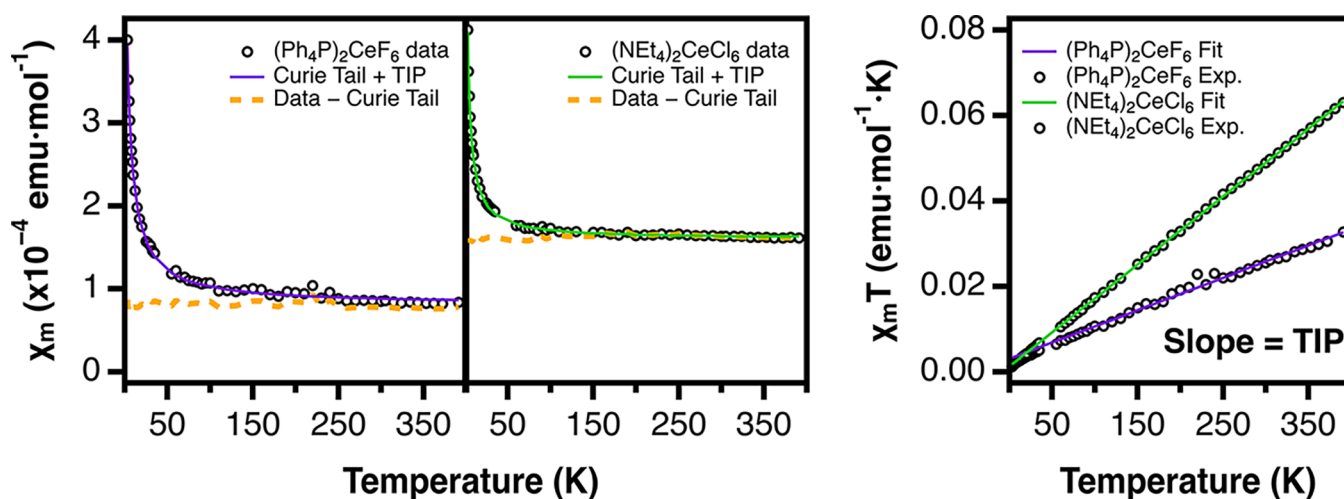
**Figure 2.** SQUID magnetometry data for $CeF_6^{2-}$ and $CeCl_6^{2-}$. The Curie–Weiss parameters are determined from the fits of the $\chi$ vs $T$ experimental data (left two windows). The $\chi T$ vs $T$ plot (right) emphasizes the difference in TIP between $CeF_6^{2-}$ and $CeCl_6^{2-}$. Experimental data points between 35 and 55 K were removed from the fit due to oxygen contamination in the instrument.

magnitude of $C$ in these samples may be assessed by assuming the impurity is Ce(III) ($C$ = 0.807 emu K/mol). By making this assumption, the amount of Ce(III) impurity is 0.27(4)% for $(Ph_4P)_2CeF_6$ and 0.14(1)% for $(Et_4N)_2CeCl_6$.

Both complexes display TIP, as observed in many compounds with formal Ce(IV) ions.[49,53−55] This behavior arises from the mixing of low lying magnetic excited states into the ground state, and the magnitude of $\chi_0$ is inversely proportional to the difference in energy between the ground state and the lowest lying excited states.[56] The TIP for $CeCl_6^{2-}$ is comparable to the published values of $1.7(2) \times 10^{-4}$ emu mol$^{-1}$ reported for $Ce(C_8H_8)_2$ and is of the same order of magnitude as many other molecular Ce(IV) compounds (Table 1).[49] The TIP for $CeF_6^{2-}$, however, is about half that

**Table 1. Summary of TIP for Selected Ce(IV) Compounds**

| compound | $\chi_0$ (emu mol$^{-1}$) | references |
|---|---|---|
| $(Ph_4P)_2CeF_6$ | $0.81(4) \times 10^{-4}$ | this work |
| $(Et_4N)_2CeCl_6$ | $1.6(2) \times 10^{-4}$ | this work |
| $Ce(C_8H_8)_2$ | $1.7(2) \times 10^{-4}$ | 49 |
| $Ce(C_8H_4(Si^iPr_3\text{-}1,4)_2)_2$ | $4.5(3) \times 10^{-4}$ | 57 |
| $Ce(trop)^a$ | $1.2(3) \times 10^{-4}$ | 55 |
| $Ce(acac)_4{}^b$ | $2.1(2) \times 10^{-4}$ | 55 |
| $Ce(tmtaa)_2{}^c$ | $2.33(6) \times 10^{-4}$ | 55 |
| $Ce\text{-}NHAr^F(TriNO_x)^d$ | $1.10(6) \times 10^{-4}$ | 53 |
| $[K(dme)_2][Ce = NAr^F(TriNO_x)]^d$ | $2.2(2) \times 10^{-4}$ | 53 |
| $K_4[Ce = O(TriNO_x)]_4{}^d$ | $4.2(5) \times 10^{-4}$ | 53 |

$^a$trop = 2-hydroxy-2,4,6-cycloheptatrienone (tropolonate). $^b$acac = 2,4-pentanedione (acetylacetonate). $^c$tmtaa = tetramethyl-dibenzotetraaza[14]annulene. $^d$TriNO$_x$ = ([(2-$^t$BuNO)-$C_6H_4CH_2]_3N)^{3-}$.

of $CeCl_6^{2-}$. Assuming a conserved state ordering, this finding can be rationalized by the greater spectral splitting of the metal orbitals by the fluoride ligand, increasing the energy gap between the ground and excited states.

**Ground State Electronic Structure Calculations.** We begin with a discussion of the ground state electronic structure of $CeF_6^{2-}$ and $CeCl_6^{2-}$ based on expectations from MO theory and quantum chemical calculations. In an $O_h$ ligand field, the Ce 5d orbitals transform as $t_{2g} + e_g$, and the 4f orbitals

transform as $a_{2u} + t_{1u} + t_{2u}$. These Ce AOs can mix with appropriate ligand-based symmetry-adapted ligand combinations (SALCs) of halide p AOs to form MOs featuring either $\sigma$ interactions ($e_g$), $\pi$ interactions ($t_{2g}$, $t_{2u}$), or both $\sigma$ and $\pi$ interactions ($t_{1u}$). The 4f orbital of $a_{2u}$ symmetry is nonbonding and represents the lowest unoccupied MO (LUMO). The remaining SALCs of $t_{1g}$ and $t_{1u}$ symmetry remain nonbonding with respect to the metal center, forming the highest occupied MOs (HOMO).

This qualitative picture of ground state electronic structure and metal–ligand bonding in $CeF_6^{2-}$ was examined computationally with three complementary approaches: density functional theory (DFT) with the B3LYP hybrid functional approximation, Hartree–Fock theory augmented by Møller–Plesset second-order perturbation theory (MP2) to treat the dynamic electron correlation, and coupled-cluster with doubles (OO-CCD). Calculations were performed on $CeCl_6^{2-}$ for comparison, which has also been the subject of in-depth computational investigations.[2,58]

Figure 3 shows quantitative MO diagrams for $CeF_6^{2-}$ and $CeCl_6^{2-}$ that were constructed based on DFT/B3LYP calculations using $O_h$ symmetry and averaged experimental Ce–L (L = F, Cl) distances of 2.152 Å (Ce–F) and 2.599 Å (Ce–Cl). Relative MO energies are shown. The HOMO energy of each complex is negative, and no significant changes in the electronic structure are obtained when a continuum embedding model with infinite dielectric is used to represent the crystal environment. From the MO diagrams some similarities and differences are noted for the two complexes. Both complexes have large HOMO–LUMO gaps of 5.99 and 3.84 eV for $CeF_6^{2-}$ and $CeCl_6^{2-}$, respectively. The HOMO–LUMO gap for $CeF_6^{2-}$ is similar to the band gap of ~6 eV of $CeO_2$ determined experimentally from X-ray photoelectron spectroscopy (XPS) and bremsstrahlung isochromat spectroscopy.[59] The nonbonding $a_{2u}$ orbital is the LUMO for both systems, but the $t_{1g}$ orbitals are the HOMOs only for $CeCl_6^{2-}$. For $CeF_6^{2-}$, the HOMOs are derived from the F-based SALCs of $t_{1u}$ symmetry, with contributions from the Ce 5p (5.4%) and Ce 4f (3.2%) orbitals. We hypothesized that the different MO ordering for $CeF_6^{2-}$ is driven by the shorter Ce–F distance vs Ce–Cl, which allows the Ce 5p inner valence orbitals to interact with occupied F $t_{1u}$ SALCs and increases their energy
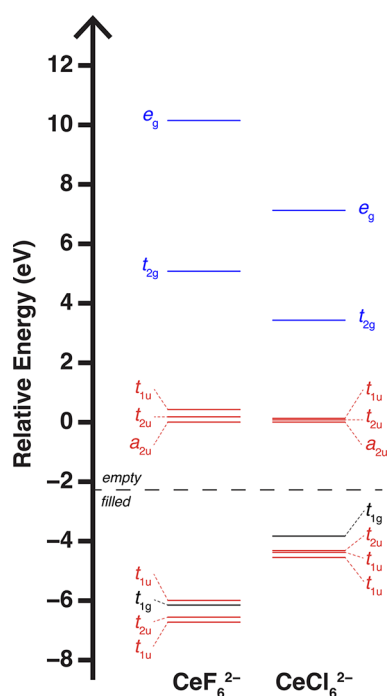
**Figure 3.** Valence MO diagrams of $CeL_6^{2-}$ (L = F, Cl), obtained from DFT/B3LYP calculations with the ANO-RCC-QZP basis sets using symmetrized crystal structures. The diagrams are aligned to each other based on the energy of the Ce 4f orbital of $a_{2u}$ symmetry, which is rigorously nonbonding for each complex. The orbitals containing Ce 4f character are shown in red, and those containing Ce 5d character are shown in blue. Nonbonding ligand SALCs are shown in black.

relative to the $t_{1g}$ orbitals. As confirmation, test calculations on $CeCl_6^{2-}$ with shortened Ce−Cl distances had the same MO ordering observed for $CeF_6^{2-}$.

Calculated electronic structure descriptors gathered in Table 2 show consistency among DFT calculations and the correlated wave function approaches, MP2 and CCSD. The OO-CCD metrics in Table 2 correspond to the "relaxed" coupled-cluster density including the desired correlation effects. Likewise, relaxed MP2 densities were used. The 4f

**Table 2. Calculated Chemical Bonding Descriptors Using Various Computational Approaches**[a]

| Bonding metric | computational method | | |
|---|---|---|---|
| | B3LYP | MP2 | OO-CCD |
| $CeF_6^{2-}$ | | | |
| $q$(Ce) | 2.09 | 2.21 | 2.32 |
| $q$(F) | −0.68 | −0.70 | −0.72 |
| $n_f$ | 0.81 | 0.70 | 0.66 |
| $n_d$ | 0.95 | 1.03 | 0.93 |
| MBO | 0.53 | 0.47 | 0.44 |
| $CeCl_6^{2-}$ | | | |
| $q$(Ce) | 1.45 | 1.35 | 1.50 |
| $q$(Cl) | −0.58 | −0.56 | −0.58 |
| $n_f$ | 1.02 | 0.91 | 0.85 |
| $n_d$ | 1.35 | 1.59 | 1.48 |
| MBO | 0.75 | 0.71 | 0.67 |

[a]Calculations were performed on $O_h$ structures with averaged experimental Ce−L (L = F, Cl) distances and ANO-RCC-QZP basis sets.

and 5d electron populations, defined as $n_f$ and $n_d$, extracted from the OO-CCD densities must be considered the most accurate among the present calculations. The $n_f$ and $n_d$ values are 0.66 and 0.93 for $CeF_6^{2-}$ and 0.85 and 1.48 for $CeCl_6^{2-}$, indicating a larger ligand-to-metal donation with Cl, especially into the Ce 5d shell. The calculated metal charges, $q$(Ce) = +2.32 for $CeF_6^{2-}$ and +1.50 for $CeCl_6^{2-}$, are quite low compared to the +4 formal charge for Ce(IV), which reflects mainly the ligand electron density donated into both the 4f and 5d shells combined. Assigning the 5d populations back to the ligands would result in metal charges of +3.25 ($CeF_6^{2-}$) and +2.98 ($CeCl_6^{2-}$), which are closer to the expected +4 charge, reflective of the 4f donation solely, and indicate a cerium oxidation state between Ce(III) and Ce(IV).

Bonding metrics obtained from the calculations compare well (Table 2). However, the DFT/B3LYP calculations provide considerably larger $n_f$ values of 0.81 ($CeF_6^{2-}$) and 1.02 ($CeCl_6^{2-}$), and larger Mayer bond orders (MBOs) of 0.53 ($CeF_6^{2-}$) and 0.75 ($CeCl_6^{2-}$). This is attributed to the delocalization error associated with common density functional approximations.[31] However, the trend of increasing ligand-to-metal donation for $CeCl_6^{2-}$ relative to $CeF_6^{2-}$ is the same. The comparison highlights the benefit of benchmarking DFT approaches to correlated wave function calculations when seeking insights into cerium electronic structure. Without the coupled-cluster reference data, it would be tempting to classify both $CeF_6^{2-}$ and $CeCl_6^{2-}$ as formally trivalent cerium complexes similar to the case of cerocene, $Ce(C_8H_8)_2$.[32,54,60] Further details are provided in the Supporting Information in the context of the dominantly single-configurational character of the ground states. It follows from the analysis that the bonding in $CeF_6^{2-}$ and $CeCl_6^{2-}$ is compatible with a description of the systems in terms of Ce(IV) accompanied by covalent bonding in the form of ligand-to-metal donation. Unlike systems such as $Ce(C_8H_8)_2$ or $Ce(\eta^8-C_8Me_6)_2$,[54,61] which require multiconfigurational treatments from the onset, the ground state electronic structure of $CeF_6^{2-}$ and $CeCl_6^{2-}$ can be safely explored with single-configurational approaches. However, the dynamic correlation is critical for a proper description of the donation and, therefore, the covalency.

**Ce $L_3$-Edge XAS.** XAS measurements at the Ce $L_3$-edge ($2p_{3/2} \rightarrow 5d_{5/2}$) were made on $CeF_6^{2-}$ to probe the amount of charge donation spectroscopically.[27−29,54,62−64] A plot of the background subtracted, normalized, and curve fit Ce $L_3$-edge XAS of $CeF_6^{2-}$ is shown in Figure 4. Charge transfer in the Ce $L_3$-edge spectra of formally tetravalent Ce compounds is often reflected by the presence of two peaks, which are commonly described using a CI model where two configurations contribute to the ground state: the tetravalent, or ionic configuration ($4f^0\underline{L}5d^0$) and the trivalent, charge transfer configuration ($4f^1\underline{L}5d^0$), where $\underline{L}$ represents a ligand hole. At the Ce $L_3$-edge, differences in the core-hole stabilization of the $4f^0\underline{L}5d^1$ and $4f^1\underline{L}5d^1$ final state configurations result in the two-peaked structure. However, inspection of the spectrum for $CeF_6^{2-}$ and its second derivative showed five main features. A low-intensity peak at 5723 eV precedes the intense, higher energy features starting with one at ca. 5730 eV, followed by a broader peak at ca. 5736 eV that is a composite of two closely spaced features, and a final high-energy peak at ca. 5741 eV. In analogy to $CeCl_6^{2-}$, whose Ce $L_3$-edge spectrum also deviated from the common two-peak structure, we attribute this structure to ligand field splitting of the 5d orbitals into $t_{2g}$ and $e_g$ components combined with the differing core-hole
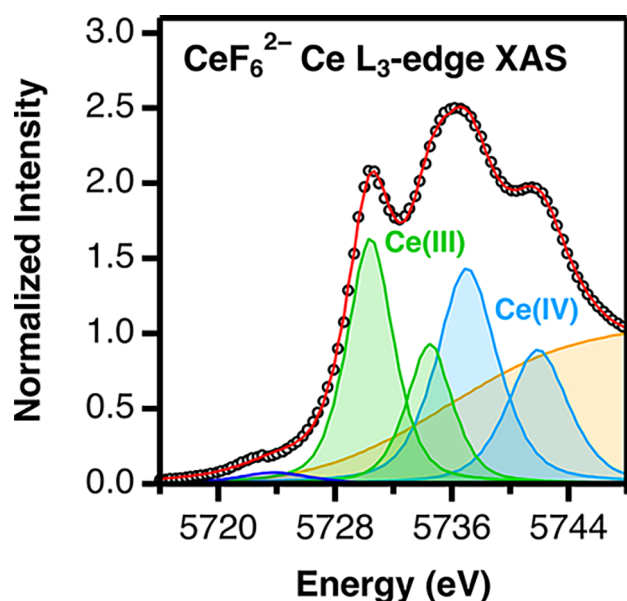
**Figure 4.** Cerium L$_3$-edge XAS spectrum of CeF$_6^{2-}$. Ce L$_3$-edge XAS features (black circles) are modeled using pseudo-Voigt functions (green and blue) and a step function (orange) to generate the total curve fit (red trace).

**Table 3. Ce L$_3$-Edge XAS Extracted $n_f$ Values**

| compound | $n_f$ | references |
|---|---|---|
| (Ph$_4$P)$_2$CeF$_6$ | 0.46(3) | this work |
| (Et$_4$N)$_2$CeCl$_6$ | 0.62(3)[a] | 2 |
| Ce(PN*)$_4$[b] | 0.47(3)[a] | 6 |
| CeO$_2$ | 0.56(4) | 62 |
| Ce(trop)$_4$ | 0.50(3) | 55 |
| Ce(acac)$_4$ | 0.51(3) | 55 |
| Ce(tmtaa)$_2$ | 0.59(3) | 55 |
| Ce−NHAr$^F$(TriNO$_x$) | 0.55(3[c] | 53 |
| [K(dme)$_2$][Ce = NAr$^F$(TriNO$_x$)] | 0.60(3)[c] | 53 |
| K$_4$[Ce = O(TriNO$_x$)]$_4$ | 0.59(3)[c] | 53 |
| Ce(C$_8$H$_8$)$_2$ | 0.89(3) | 54 |
| Ce($\eta^8$-C$_8$Me$_6$)$_2$ | 0.87(5) | 61 |

[a]To make accurate comparisons, the experimental data reported previously was curve-fit using a model similar to the one used for (Ph$_4$P)$_2$CeF$_6$. See the Supporting Information for complete details. [b]PN* = [NP(1,2-bis-$^t$Bu-diamidoethane)(NEt$_2$)]$^-$. [c]These values were reported as $n_{f0}$, and have been converted to $n_f$ by assuming $n_f$ = 1 − $n_{f0}$.

stabilizations. To quantify these two effects, a fitting model was developed based on 5 pseudo-Voigt functions and a step-like function. Within this model, the peak at ca. 5736 eV is a composite of the Ce(III) e$_g$ and Ce(IV) t$_{2g}$ components. To prevent unphysical fit results owing to these overlapping features, the widths of the crystal field components were constrained to be equal within each final state subconfiguration. This assignment of two features in the composite peak at ca. 5736 eV is supported by the presence of two minima in that energy region of the second derivative of the experimental spectrum.

The relative amount of Ce(III) 4f$^1$$\underline{L}$5d$^0$ character in the ground-state wave function is estimated by summing the areas of the peaks associated with Ce(III) and Ce(IV) components and taking the ratio of the Ce(III) area to the Ce(III) + Ce(IV) area, A$_{3+}$/(A$_{3+}$ + A$_{4+}$). This ratio gives the $n_f$ value, representing the number of f electrons on the formally Ce(IV) center in the ground state. However, it is likely that this should be taken as the lower limit of $n_f$ due to a small Ce(II) component that cannot be resolved from the Ce(III) component.[32,48,55] By this methodology, the extracted fraction of Ce(III) based on the fit was 0.46(3), with the error estimated by the profiling method (see Supporting Information). This $n_f$ is among the smallest reported to date for formal Ce(IV) compounds (Table 3). It is most notably smaller than those of Ce(C$_8$H$_8$)$_2$ ($n_f$ = 0.89(3)),[54] Ce($\eta^8$-C$_8$Me$_6$)$_2$ ($n_f$ = 0.87(5)),[61] CeO$_2$ ($n_f$ = 0.56(4)),[28,55,62] and CeCl$_6^{2-}$ ($n_f$ = 0.62(3)), and is comparable to that of Ce(NP(1,2-bis-$^t$Bu-diamidoethane)(NEt$_2$))$_4$ ("Ce(PN*)$_4$") ($n_f$ = 0.47(3)).[6,65] The latter two comparisons were refit to a model equivalent to the present one in order to make accurate comparisons.

**Ab Initio Calculation of the Ce L$_3$-Edge Spectra.** CeF$_6^{2-}$ and CeCl$_6^{2-}$ were subjected to wave function theory (WFT) calculations for determining the Ce L$_3$-edge structure. As for the previous calculations, octahedral structures with averaged experimental bond lengths were used. Following previous work on ab initio XAS,[32,66,67] we performed a series of restricted active space self-consistent field (RAS-SCF) calculations for the valence and the core excited states targeted in the XAS experiments, followed by multireference second-order perturbation theory (PT2) calculations for the dynamic electron correlation.

The two-peak Ce L$_3$-edge structure arises from 2p → 5d core excitations grouped into Ce(III) 4f$^1$$\underline{L}$5d$^1$ and Ce(IV) 4f$^0$$\underline{L}$5d$^1$ final-state subconfigurations. A recent ab initio analysis of such core excited states for the cases of CeO$_2$ vs Ce(C$_8$H$_8$)$_2$ can be found in ref 32. The transitions usually give two peak groups in the L$_3$-edge, groups A (Ce(III)) and B (Ce(IV)), with transition types A at lower energy. The A/B intensity ratio relates to the Ce(III) vs Ce(IV) contributions to both the ground state wave function and the relevant wave functions of the core excited states. In the case of formally tetravalent compounds, these Ce(III) and Ce(IV) contributions are modulated by the ligand np to Ce 4f donation in the ground states, which typically shows up in calculations via ligand−metal orbital hybridization. In the present CeL$_6^{2-}$ (L = F, Cl) cases, Ce(III) vs Ce(IV) is modulated via the donation to the metal 4f AOs in the t$_{1u}$ and t$_{2u}$ species. Therefore, the Ce L$_3$-edge spectra of CeF$_6^{2-}$ and CeCl$_6^{2-}$ were calculated separately for transitions involving the t$_{1u}$ and the t$_{2u}$ MO sets in order to overcome the computational complexity, and the total intensity from the two calculations was combined. With the chosen 2.0 eV Lorentzian broadening of the individual transitions, the calculated Ce L$_3$-edge structures reproduce the experimental counterparts very well (Figure 5).

The calculated L$_3$-edge spectra depend mainly on the adequate description of the acceptor Ce(5d) MOs, the overall bonding involving the Ce(4f) shell, and the overall energy splitting of the orbitals. They depend less on the balance of the donation present in the t$_{1u}$ vs t$_{2u}$ MOs than the ligand K-edges (*vide infra*). The calculated spectra shown in Figure 5 clearly show that both the t$_{1u}$ and t$_{2u}$ bonding and antibonding MO pairs are needed to reproduce the experimental envelopes: they both generate Ce(III) and Ce(IV) (A vs B group) final-state configurations. Apart from this, the interpretation of these spectra follows closely that of CeO$_2$:[32] each peak group, A and B, is split by the ligand field splitting of the Ce(5d) orbitals, such that 3 or 4 peaks are resolved in the experimental
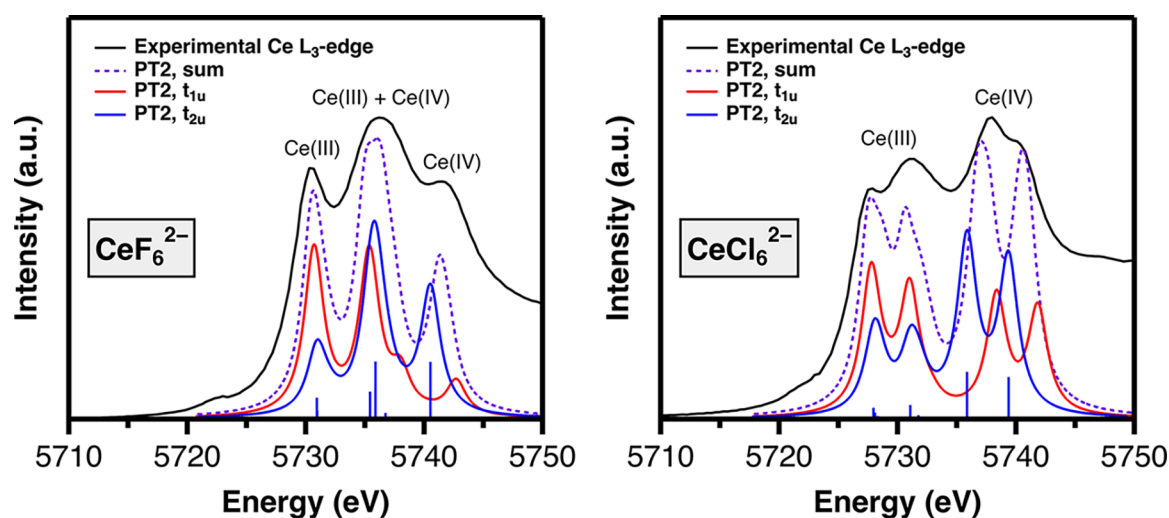
**Figure 5.** Calculated vs experimental Ce $L_3$-edge XAS for $CeF_6^{2-}$ and $CeCl_6^{2-}$. To avoid clutter, "stick" transitions are only shown for the RAS-PT2 spectra calculated with the ligand and the metal-centered $t_{2u}$ orbitals. The calculated spectral envelopes were generated with 2.0 eV Lorentzian broadening of the individual transitions.

**Table 4. Natural Configurations for the Ground State and the Four Core Excited State Transitions (Blue Sticks in Figure 3) Responsible for Intensities in the Ce $L_3$-Edge Structures of the $CeL_6^{2-}$ Systems (L = F, Cl)**[a]

| system | param. | GS | A.1 | A.2 | B.1 | B.2 |
|---|---|---|---|---|---|---|
| $CeF_6^{2-}$ | config. | $L^{5.98}f^{0.02}$ | $[L^{5.15}f^{0.85}]t_{2g}^1$ | $[L^{5.19}f^{0.81}]e_g^1$ | $[L^{5.74}f^{0.26}]t_{2g}^1$ | $[L^{5.75}f^{0.25}]e_g^1$ |
| | $\Delta E$, eV | | 0.00 | 4.47 | 4.94 | 9.59 |
| $CeCl_6^{2-}$ | config. | $L^{5.88}f^{0.12}$ | $[L^{5.04}f^{0.96}]t_{2g}^1$ | $[L^{5.06}f^{0.94}]e_g^1$ | $[L^{5.91}f^{0.09}]t_{2g}^1$ | $[L^{5.91}f^{0.09}]e_g^1$ |
| | $\Delta E$, eV | | 0.00 | 3.08 | 7.90 | 11.39 |

[a]The Ce(III) $4f^1\underline{L}5d^1$ and Ce(IV) $4f^0\underline{L}5d^1$ configurations were generated with the $t_{2u}$ orbitals. A.1 & A.2 and B.1 & B.2 label the two transitions ("sticks") under peak groups A and B shown in Figure 3. Note that the 4f populations extracted from the RAS calculations are uniformly smaller than those given in Table 2 because of a lack of dynamic correlation and differences in the way the populations were obtained. However, the spectral features are mainly indicative of the relative state assignments.

spectrum. The larger the 5d $t_{2g}-e_g$ splitting is, the closer is the high-energy peak in group A to the low-energy peak in group B. For $CeF_6^{2-}$, which has the larger 5d splitting, the higher-energy A subpeak overlaps with the lower-energy B subpeak around 5736 eV. These peaks remain separated for $CeCl_6^{2-}$, which has a smaller 5d $t_{2g}-e_g$ splitting. Another conclusion from Figure 5 is that $t_{1u}$ contributes preferentially over $t_{2u}$ in peak group A. The opposite is the case for peak group B. To support the assignment of the Ce $L_3$-edge peaks, we provide in Table 4 the natural orbital populations for the intense core excited states (involving the $t_{2u}$ MO set) shown as "sticks" in Figure 3. The natural populations were calculated from the configurations and their corresponding weights in the wave functions expressed in the state-averaged orbitals. Conveniently, for each case, these orbitals turned out to be localized in the $t_{1u}$ and $t_{2u}$ symmetry species (irreducible representations or "irreps") such that they can be labeled straightforwardly as "L" for the ligand-based np combination and "f" for a Ce(4f) AO. It follows that for each state, the 4f population is indicative of the $n_f$ value of Ce, which in turn can be used to assign its oxidation number.

From the data in Table 4, we conclude that the ground states are best described as Ce(IV) because the 4f population is relatively small. The 4f population increases from 0.02 (F) to 0.12 (Cl), thus evidencing increasing ground state donation into the 4f orbitals in $CeL_6^{2-}$. The same trend holds when analyzing the data obtained with the $t_{1u}$ MOs (not shown in Table 4). The excited states for transitions A.1 and A.2 (i.e., the

first and second transition under the first peak group A in Figure 3) have nearly one electron the Ce 4f shell, whereas the excited states of transitions B.1 and B.2 (first and second transition under the peak group B in Figure 3) have close to zero 4f population. In other words, to summarize this part of the study, the calculations confirm that peak group A is associated with Ce(III) core excited states, peak group B with Ce(IV) core excited states, both peaks are split by the 5d ligand field splitting but lead to overlapping bands in the fluoride complex, and the ground state of both complexes is described by Ce(IV) with some electron donation from the ligands.

**Ce $M_{5,4}$-Edge and F K-Edge XAS.** A scanning transmission X-ray microscope (STXM) was utilized to obtain F K-edge and Ce $M_{5,4}$-edge XAS from micron-scale crystals of $(Ph_4P)_2CeF_6$. An X-ray image of representative crystallites of $(Ph_4P)_2CeF_6$ alongside STXM elemental distribution maps of F and Ce is shown in Figure 6. Small droplets of $(Ph_4P)_2CeF_6$ in MeCN were allowed to evaporate on $Si_3N_4$ windows, which formed a large number of small crystallites in a compact area that were suitable for STXM raster scans. By selecting thin crystals (ca. 0.5–1.0 $\mu$m) with a large surface area (ca. 50–100 $\mu m^2$), this approach was effective at distributing the effect of radiation damage over a larger area. Radiation damage was not detected, and high-quality F K-edge and Ce $M_{5,4}$-edge XAS were obtained by averaging data sets from multiple independent crystals.
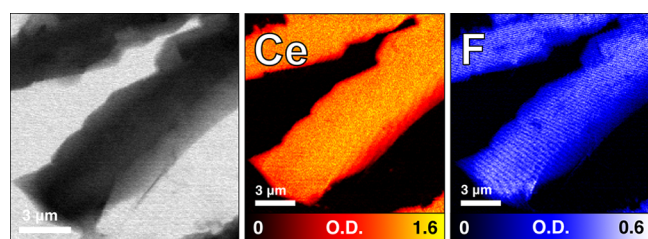
**Figure 6.** STXM image and elemental distribution maps of F and Ce on representative crystallites of $(Ph_4P)_2CeF_6$. The optical density in the Ce map is higher than that in the F map owing to the greater intrinsic intensity of the Ce $M_{4,5}$-edge alongside the higher mass percent of Ce in the salt.

*Ce $M_{4,5}$-Edge XAS and Atomic Multiplet Simulation.* Ce $M_{4,5}$-edge XAS probes the electric-dipole-allowed transitions from core 3d orbitals into the valence 4f orbitals, providing a unique opportunity to directly probe the 4f shell. Typical Ln $M_{4,5}$-edge spectra show well-defined $M_4$- and $M_5$-edges in addition to multiplet structure that is characteristic of the number of 4f-electrons.[68−70] This technique has been used extensively to investigate partial 4f-orbital occupancies in lanthanide oxides, halides, and intermetallics, among other compounds.[23,71−75] The Ce $M_{4,5}$-edge spectrum for $CeF_6^{2−}$ is shown in Figure 7, and the associated peak energies and
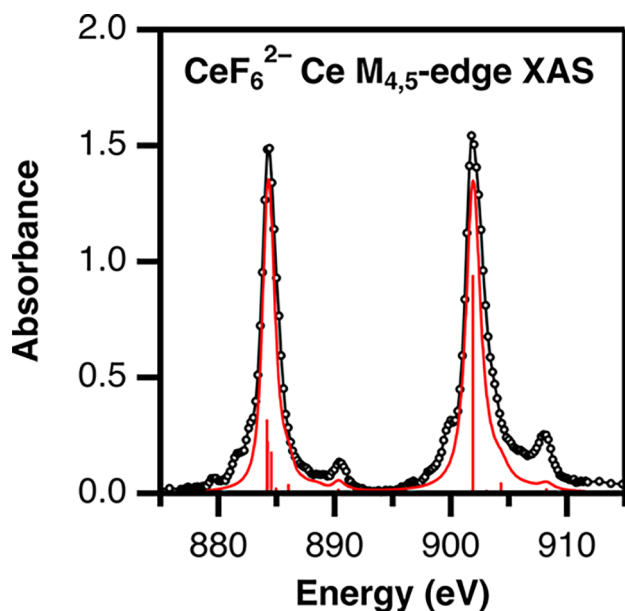


**Figure 7.** Comparison of the experimental (black) and CI calculated (red) Ce $M_{4,5}$-edge spectrum for $CeF_6^{2−}$.

branching ratios are shown in Table 5. In comparison to $CeCl_6^{2−}$, both the $M_5$ and $M_4$-edges are shifted to higher

energy in $CeF_6^{2−}$. In XAS, an edge shift to higher energy is often attributed to stabilized core orbitals due to an increase in positive charge on the absorbing atom.[76]

The $M_{4,5}$-edge spectrum of $4f^0$ Ce(IV) compounds is expected to be qualitatively similar to that of $4f^0$ La(III) compounds, whose $M_{4,5}$-edge spectra only have two intense features.[68] The presence of satellite peaks like those observed for $CeF_6^{2−}$ has been attributed to excited state charge transfer enabled by metal−ligand orbital mixing.[78] To relate these satellite features to the ground state electronic structure, a spectral simulation was performed using the Theo Thole multiplet code, with modifications by Ogasawara, as maintained and used by the CTM4XAS program.[79] This code is based on the charge transfer multiplet (CTM) model and explicitly accounts for core-hole effects that are not considered in most DFT calculations. In particular, core-hole-induced charge transfer in the excited state is included, allowing us to simulate the satellite features described above. Input parameters used previously for $CeCl_6^{2−}$ were used for the atomic multiplet component of the calculation for $CeF_6^{2−}$, except for the core-hole spin−orbit coupling, which was reduced to 98% (vs 99% for $CeCl_6^{2−}$).[2] For the charge transfer component, we are concerned with the following parameters:

- $\Delta E_{gs}$, the ground state charge transfer energy (4.6 eV)
- $T_{gs}$, the ground state effective hopping integral (0.92 eV)
- $\Delta E_{fs}$, the final state charge transfer energy (1.8 eV)
- $T_{fs}$, the final state effective hopping integral (0.92 eV)

The values used in this calculation are given in parentheses. The result of this calculation for $CeF_6^{2−}$ is shown alongside the experimental spectrum in Figure 7. Starting from the values used for $CeCl_6^{2−}$, $\Delta E_{gs}$ was set by adding the difference in the HOMO−LUMO energy gap between $CeF_6^{2−}$ and $CeCl_6^{2−}$ (2.1 eV, from ground state computations) to the $\Delta E_{gs}$ for $CeCl_6^{2−}$. Then, $\Delta E_{fs}$ was determined by incrementally increasing the value from $CeCl_6^{2−}$ until the spectral profiles of the main edges and satellite features were in good agreement with experiment. Finally, in order to confine the number of free variables, $T_{gs}$ and $T_{fs}$ were set equal to each other, and their value was varied until the energy splitting between the main edges and satellite features were also in good agreement with experiment. The complete input and output files may be found in the Supporting Information.

The charge transfer calculation produces the simulated spectrum by first computing a ground state wave function composed of Ce(III) $3d^{10}4f^1\underline{L}$ and Ce(IV) $3d^{10}4f^0L$ components. The weight of the Ce(III) component, 0.19 is taken as the computed Ce $n_f$. This value is lower than the value of 0.25 calculated previously based on the $M_{5,4}$-edge spectrum of $CeCl_6^{2−}$.[2] Both $n_f$ are much lower than those found via $L_3$-edge XAS, which likely reflects the limitations of the CTM model. However, the lowering of the $n_f$ value from $CeCl_6^{2−}$ to $CeF_6^{2−}$ based on $M_{5,4}$-edge XAS and CTM calculations is

**Table 5. Comparison of Experimental Ce $M_{4,5}$-Edge Peak Energies and Intensities**

| | peak energies (eV) | | | | peak splitting (eV) | | branching ratio |
|---|---|---|---|---|---|---|---|
| | $M_5$-edge | | $M_4$-edge | | sat−main | $M_5$−$M_4$ | $A_5/(A_5 + A_4)$ |
| | main | satellite | main | satellite | avg | main | |
| $CeF_6^{2−}$ | 884.2 | 890.4 | 901.8 | 908.0 | 6.2 | 17.6 | 0.50(2)[a] |
| $CeCl_6^{2−b}$ | 883.7 | 888.6 | 901.6 | 906.4 | 4.9 | 17.9 | 0.48(2) |

[a]Peak areas were calculated by integrating the second derivative graph of the data above zero.[77] [b]Chloride data from ref 2.

consistent with the trend in $n_f$ values observed at the $L_3$-edge, which indicates decreased ligand donation in $CeF_6^{2-}$.

*F K-Edge XAS and Spectral Simulation.* The background-subtracted, normalized, and fit F K-edge spectrum of $CeF_6^{2-}$ obtained using a STXM is shown in Figure 8. The pre-edge
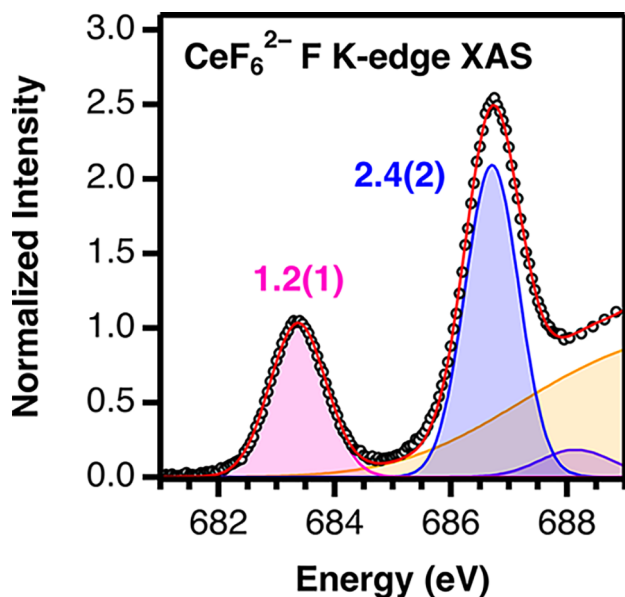


**Figure 8.** Normalized fluorine K-edge XAS spectrum of $CeF_6^{2-}$. F K-edge XAS pre-edge features (black circles) are modeled using Gaussian functions (pink, blue, and purple) and a step function (orange) to generate the total curve fit (red trace). The spectral intensities (pink and blue numbers) are given by the areas under the Gaussian functions.

region of the spectrum contains two features below 690 eV, which were modeled using two symmetrically constrained Gaussian functions at 683.4 and 686.7 eV (see Experimental Section).[80−82] Based on the ground-state electronic structure model for $CeF_6^{2-}$ described above, and on the previously reported assignments of the Cl K-edge spectra for $CeCl_6^{2-}$ and $UCl_6^{2-}$,[2,81] we assigned the lowest energy feature at 683.4 eV

to coincident transitions from the F 1s orbitals into the Ce−F antibonding orbitals of $t_{1u}$ and $t_{2u}$ symmetry. The individual transitions are not resolved by F K-edge XAS, presumably due to the weak ligand field splitting of 4f orbitals. Moving to higher energy, the feature at 686.7 eV represents the transition into the Ce−F antibonding orbitals of $t_{2g}$ symmetry. No single feature attributable to transitions into the $e_g$ orbitals were observed, which are presumably not resolved from other transitions in the rising edge region.

Figure 9 shows ligand K-edge spectra for $CeF_6^{2-}$ and $CeCl_6^{2-}$ that were calculated within the framework of WFT approaches, similar to the previously discussed $L_3$-edge spectra calculations. For both systems, the relative intensities and energetic splitting of the two pre-edge features are in good agreement with experiment. The first pre-edge peak arises from core transitions into the Ce 4f antibonding orbitals of $t_{1u}$ and $t_{2u}$ symmetry, with the transition into the $t_{2u}$ being slightly more intense. The second and third peaks are assigned to transitions into the Ce 5d orbitals of $t_{2g}$ and $e_g$ symmetry, respectively. Based on these data, however, it is difficult to conclude whether the $t_{2u}$ MOs have more F 2p or Cl 3p character compared to the $t_{1u}$ MOs, as the orbital optimization in these calculations leads to rather strongly localized orbitals.

## ■ EVALUATION OF ORBITAL MIXING (EVALUATION OF F COVALENCY)

The F K-edge XAS results described above show that the F 2p orbitals engage in bonding with both the Ce 4f and 5d orbitals. Because the intensities of the F K-edge pre-edge transitions are weighted by the amount of F 2p orbital character in the acceptor orbitals, the orbital mixing can be determined experimentally and compared with expectations from the ground state calculations. Spectral intensities were determined by taking the area under the Gaussian functions that are fit to the experimental spectra, which provides a value of 1.2(1) for the function attributed to F 1s → $t_{1u}$ + $t_{2u}$ transitions and 2.4(2) for the function attributed to F 1s → $t_{2g}$ transitions.

For the $t_{2g}$ orbitals, the ligand p-orbital character $(\lambda_{t_{2g}}^2)$ is calculated according to the general equation for ligand K-edge intensity
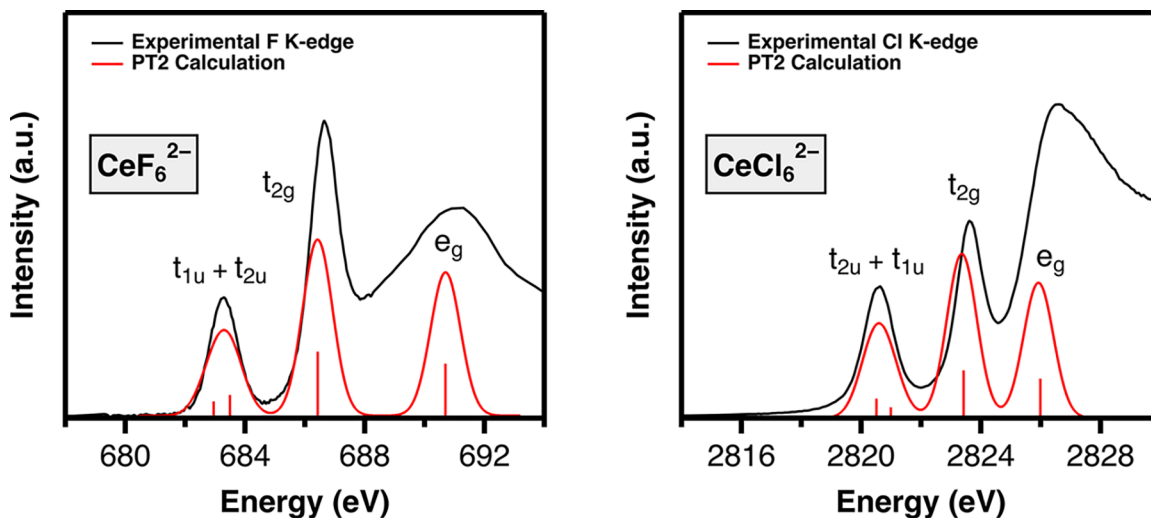


**Figure 9.** Calculated vs experimental ligand K-edge XAS for $CeF_6^{2-}$ and $CeCl_6^{2-}$, from RAS-PT2 wave function calculations with quantitative assignments of the final state orbitals. The calculated spectra are obtained with a 0.5 eV Gaussian broadening of the individual transitions. The calculated spectra were shifted and scaled to match the experimental envelopes at the first pre-edge peak.

$$I_{1s \to \psi^*} = \frac{h}{N} \lambda^2 I_{1s \to np} \qquad (2)$$

where $h$ is the number of holes in the acceptor orbital set (6 for $t_{2g}$), $N$ is the number of absorbing atoms bound to the metal (6 for $CeL_6{}^{2-}$), $n$ is the principal quantum number of the valence p-orbitals for a given ligand, and $I_{1s \to np}$ is the intrinsic intensity for the 1s → np transition of the absorbing atom.[36] For Cl K-edge measurements, the value of 7.0(2) for $I_{1s \to np}$ has been well-established by Solomon and co-workers using $CuCl_4{}^{2-}$.[34,37] For these F K-edge measurements, the F K-edge spectrum of $F_2$ gas is used to determine a value of 16.3(8) for $I_{1s \to np}$.[83] With these values, we find $\lambda^2_{t_{2g}} = 0.15(1)$ for $CeF_6{}^{2-}$ and $\lambda^2_{t_{2g}} = 0.12(1)$ for $CeCl_6{}^{2-}$. Since the lowest energy pre-edge feature gains intensity from two separate transitions involving the $t_{1u}$ and $t_{2u}$ orbitals that are not independently resolved in the F K-edge spectrum, the average ligand p-orbital character in these orbitals ($\lambda^2_{avg}$) was calculated according to eq 3

$$I_{1s \to t_{1u}} + I_{1s \to t_{2u}} = I_{1s \to t_{1u} + t_{2u}} = 2\lambda^2_{avg} I_{1s \to np} \qquad (3)$$

A derivation of this equation starting from eq 2 is provided in the Supporting Information. Using eq 3, a $\lambda^2_{avg}$ of 0.037(4) is calculated for $CeF_6{}^{2-}$, which can be compared to the value of 0.050(5) determined using Cl K-edge data published previously for $CeCl_6{}^{2-}$ (reported originally as $\lambda^2_{t_{1u}} + \lambda^2_{t_{2u}}$).[2]

The consequence of orbital mixing in the $t_{1u}$ and $t_{2u}$ MOs is donation of ligand electron density into the 4f orbitals. For the Ce $M_{5,4}$ and $L_3$-edge XAS measurements on $CeF_6{}^{2-}$ and $CeCl_6{}^{2-}$, the electronic structure was described with localized orbitals using a CI model, and the extent of donation bonding was reflected by the value $n_f$, or the weight of the Ce(III) configuration (vide infra).[105] Comparison between the CI and MO models is achieved by $n_f = 12\lambda^2_{avg}$, where 12 reflects the number of bonding electrons in the $t_{1u}$ and $t_{2u}$ orbital sets. Results of this calculation and comparison with other measurements are provided in Table 6. The values of $n_f$

**Table 6. Comparison of Experimental and Calculated Ce $n_f$ Values**

|  | $CeF_6{}^{2-}$ | $CeCl_6{}^{2-}$ |
|---|---|---|
| exp. ligand K-edge | 0.44(4) | 0.60(6) |
| exp. Ce $L_3$-edge | 0.46(3) | 0.62(3) |
| CTM Ce $M_{4,5}$-edge | 0.19 | 0.25 |
| OO-CCD ground state | 0.66 | 0.85 |

determined using $\lambda^2_{avg}$ from F and Cl K-edge XAS were 0.44(4) for $CeF_6{}^{2-}$ and 0.60(6) for $CeCl_6{}^{2-}$. These values are within error of those determined with Ce $L_3$-edge XAS, 0.46(3) for $CeF_6{}^{2-}$ and 0.62(3) for $CeCl_6{}^{2-}$. Moreover, this trend is consistent with that determined from OO-CCD ground state calculations (0.66 for $CeF_6{}^{2-}$ and 0.85 for $CeCl_6{}^{2-}$). While the calculated values are higher than those determined experimentally, both approaches show $CeCl_6{}^{2-}$ to have an $n_f$ about 0.2 higher than $CeF_6{}^{2-}$. Intermediate to the $CeF_6{}^{2-}$ and $CeCl_6{}^{2-}$ experimental $n_f$ values is that reported for $CeO_2$, 0.56(4),[62] and much higher is that of cerocene, 0.89(3).[54] This comparison reveals a general trend between the electronegativity of the Ce(IV)-bound atom and the Ce(IV) $n_f$ value. However, this trend may not hold in the case

of novel ligands or coordination geometries, as in the case of Ce(PN*)$_4$ with an $n_f$ of 0.47(3).[6,65]

To a first approximation, the greater amount of donation bonding in $CeCl_6{}^{2-}$ can be rationalized simply by the fact that the Cl 3p orbitals are higher in energy, and thus closer in energy to the Ce 4f orbitals.[84] However, the amount of orbital mixing is proportional not only to the inverse orbital energy difference, but also the orbital overlap.[38] Using the second-order model applied by Burdett to transition metal complexes alongside the Wolfsberg–Helmholz approximation,[40,85] $\lambda^2_{avg}$ can be related to orbital overlap ($S^2_{avg}$) according to

$$\lambda^2_{avg} = \frac{S^2_{avg} E_M E_X}{(E_M - E_X)^2} \qquad (4)$$

where $E_M$ and $E_X$ are the metal and ligand AO energies, respectively. $E_X$ is defined exactly as the negative of the first ionization potential of the halogen atom (−17.4 eV for F and −12.9 eV for Cl),[86] as described by Koopmans' theorem,[87] and $E_M$ is estimated as the negative fourth ionization potential of Ce divided by four (−9.2 eV).[86] With these energies and the $\lambda^2_{avg}$ determined from ligand K-edge XAS, we find $S^2_{4f,avg} = 0.016(2)$ for $CeF_6{}^{2-}$ and $S^2_{4f,avg} = 0.0058(6)$ for $CeCl_6{}^{2-}$. These values show that the Ce−F bonds in $CeF_6{}^{2-}$ are characterized by significantly more Ce 4f and F 2p overlap compared with the amount of Ce 4f and Cl 3p overlap in the Ce−Cl bonds of $CeCl_6{}^{2-}$. We note that greater 5f-orbital overlap with the halide ligands in $UF_6{}^{n-}$ compared with $UCl_6{}^{n-}$ ($n = 1, 2$) has been observed previously by fitting 5f−5f transitions within a modified crystal field model.[88] The $\lambda^2_{t_{2g}}$ values can be used to estimate $S^2_{t_{2g}}$ relative to $S^2_{4f,avg}$ as a function of the value of $E(Ce\ 5d)$. While the Ce 5d orbitals are expected to be 1−2 eV higher in energy than the 4f,[89] an experimental value corresponding to the energy of the 5d orbitals of the $4f^0 5d^0$ Ce(IV) ion is not known. As shown in Figure S11, at values of $E(Ce\ 5d) \geq E(Ce\ 4f)$, overlap in the $t_{2g}$ MOs is greater than that in the 4f MOs for both $CeF_6{}^{2-}$ and $CeCl_6{}^{2-}$. Using the energy of the Hf(IV) 5d orbitals (−8.3 eV) as a proxy for that of the Ce(IV) 5d orbitals, we estimate the value of $S^2_{t_{2g}}$ at 0.084(8) for $CeF_6{}^{2-}$ and 0.024(2) for $CeCl_6{}^{2-}$.

The presence of greater ligand overlap with the 4f orbitals In $CeF_6{}^{2-}$ relative to $CeCl_6{}^{2-}$ may seem counterintuitive since the other metrics of bonding, $\lambda^2_{avg}$ and $n_f$, suggest that $CeF_6{}^{2-}$ has both less orbital mixing and less ligand-to-metal charge donation than $CeCl_6{}^{2-}$. However, these concepts are not mutually exclusive. The $\lambda^2_{avg}$ determined here account for the electron density on the ligand atoms plus half that in the region of metal−ligand orbital overlap. A large overlap can be accompanied by low internuclear charge buildup if the mixing coefficient is sufficiently low, as is the case here (see Supporting Information). While overlap in $CeF_6{}^{2-}$ does not lead to much greater orbital mixing, it plays an important role in the energetic stabilization of bonding (or destabilization of antibonding) orbitals, for which $\Delta E_{bonding} \approx S^2 E_M^2/(E_L - E_M)$.[40,90] Therefore, it is likely that the greater overlap in the Ce−F bond of $CeF_6{}^{2-}$ enhances the contribution of orbital mixing to overall bond stabilization relative to the Ce−Cl bond of $CeCl_6{}^{2-}$.

## ■ CONCLUSIONS

In summary, $CeF_6{}^{2-}$ was synthesized as $(Ph_4P)_2CeF_6$ and initially characterized by optical and vibrational spectroscopy,

which were not sufficient to evaluate the extent of metal–ligand orbital mixing. With SQUID magnetometry, we showed that $CeF_6^{2-}$ displays less TIP than $CeCl_6^{2-}$ and other representative coordination compounds of Ce(IV), hinting at a departure from typical Ce(IV) electronic structure. Then, a broad suite of X-ray spectroscopic and theoretical tools was used to show operative 4f orbital mixing in the Ce–F bonds in $CeF_6^{2-}$. Excellent, quantitative agreement was observed between the experimental F K-edge and Ce $L_3$-edge data and computational metrics of bonding, which provides confidence in the reliability of the results. Ground state electronic structure calculations and ab initio spectral simulations suggest the 4f orbitals engage in both $\sigma$ and $\pi$-bonding interactions involving the $t_{1u}$ and $t_{2u}$ orbitals. F K-edge XAS was used to evaluate mixing of F 2p character into the $t_{1u}$ and $t_{2u}$ orbital sets, which represent F 2p → Ce 4f electron donation. The amount of F 2p → Ce 4f electron donation ($n_f$) for $CeF_6^{2-}$ determined using F K-edge XAS (0.44(4)) was found to be equivalent to that determined from Ce $L_3$-edge XAS (0.46(3)). Comparison with $CeCl_6^{2-}$ showed that $CeF_6^{2-}$ has less electron donation. In fact, $CeF_6^{2-}$ appears to be among the most ionic Ce(IV) compounds reported to-date.

The increased metal–ligand orbital mixing, $\lambda_{avg}^2$, in $CeCl_6^{2-}$ versus $CeF_6^{2-}$ is rationalized by its inverse dependence on the difference between the Ce 4f and ligand AO energies ($E_M - E_L$), which is smaller for $CeCl_6^{2-}$ (~3.7 eV) than in $CeF_6^{2-}$ (~8.2 eV). Experimentally determined values for metal–ligand orbital overlap were calculated using these values, which showed greater orbital overlap in the Ce–F bonds compared to the Ce–Cl bonds. Such a result is, perhaps, counterintuitive since the other metrics of metal–ligand bonding show greater orbital mixing ($\lambda^2$) and Cl 3p → Ce 4f charge donation ($n_f$) in $CeCl_6^{2-}$. Overlap in $\pi$ interactions is known to be smaller for 3p versus 2p elements,[91–93] and thus better overlap in $CeF_6^{2-}$ may be a consequence of the $O_h$ symmetry (6 $\sigma$ and 12 $\pi$ interactions involving f-orbitals[94]) and better size match between Ce 4f and F 2p orbitals. Since the $t_{2g}$ orbital is solely $\pi$-bonding, the greater $\lambda_{t_{2g}}^2$ and estimated $S_{t_{2g}}^2$ in $CeF_6^{2-}$ vs $CeCl_6^{2-}$ support that enhanced $\pi$-bonding is enabled by the F 2p orbitals. Ultimately, the enhanced overlap in $CeF_6^{2-}$ is more than offset by the larger difference in orbital energies ($E_M - E_L$), such that $CeCl_6^{2-}$ has the most orbital mixing. However, the energetic stabilization due to 4f-orbital mixing is likely larger in $CeF_6^{2-}$ due to the extra dependence of MO energy on overlap, $\Delta E_{bonding} \approx S^2 E_M^2 / (E_L - E_M)$.[40,90] It is important to note that this behavior differs from the counterintuitive orbital mixing discussed by Whangbo and Hoffman, wherein an out-of-phase antibonding orbital is lower in energy than the corresponding in-phase bonding orbital.[95] The relative influence of overlap vs energy matching remains strongly debated.[96] Conceptually, a full understanding of the relative importance of overlap vs AO energy matching requires, among other aspects, unambiguous definitions of AOs and their energies for the purpose of the bond formation, alongside a careful comparison among them for free atoms, free ions, and the atoms in the complexes. Work along these lines is under way in our laboratories, and the availability of experimentally derived overlaps for the systems studied here will greatly assist these future analyses. Further future work will use the approach described herein to directly probe overlap in other d- and f-block fluorides, chlorides, and bromides.

## ■ EXPERIMENTAL SECTION

**General Considerations.** Unless otherwise noted, all manipulations were performed using standard Schlenk techniques or in an MBraun glovebox under an atmosphere of argon. All glassware was dried at 150 °C for at least 12 h. Propylene carbonate (99%, Thermo Scientific) was vacuum distilled and degassed by sparging with argon for 20 min. Acetonitrile (MeCN) (Fisher) was purified by passage through a column of activated alumina prior to use. Acetone (Sigma-Aldrich, ACS grade) was used as received. Cerium(IV) fluoride (Sigma-Aldrich) and Et$_4$NF·$x$H$_2$O (Thermo Scientific) were used as received. $(Et_4N)_2CeCl_6$ was prepared as previously described.[2] Samples for UV–vis spectroscopy were measured as solutions in MeCN on a Cary 5G Spectrophotometer from 200 to 2000 nm with 1 nm step sizes. Samples for IR spectroscopy were prepared as nujol mulls with KBr plates and measured with a Bruker Vertex 80v spectrometer. Raman data was collected on JASCO NRS-5500 Raman Spectrometer using a 532 nm laser. More details on the Raman sample preparation and collection parameters are found in the Supporting Information.

**Single Crystal X-ray Crystallography.** In a dry argon glovebox, single crystals of $(Ph4P)_2CeF_6$ were coated in Paratone-N oil. A suitable crystal was selected and mounted on a MiTeGen 100 $\mu$m Dual-Thickness MicroLoop for measurement on a Rigaku XtaLAB Synergy, Dualflex, HyPix diffractometer using Mo K$\alpha$ radiation ($\lambda$ = 0.71073 Å). The crystal was kept at 100.0(5) K during data collection. CrysAlisPro[97] was used from data collections and processing, including multiscan absorption correction applied using the SCALE3 ABSPACK scaling algorithm within CrysAlisPro. With Olex2,[98] the structure was solved with the SHELXT[99] structure solution program using Intrinsic Phasing and refined with the SHELXL[100] refinement package using least-squares minimization. Thermal parameters for all non-hydrogen atoms were refined anisotropically.

**Synthesis of (Ph$_4$P)$_2$CeF$_6$.** The synthesis of the $(Et_4N)_2CeF_6$·6H$_2$O intermediate was adapted from that reported by Balasekaran et al.[42] CeF$_4$ (507.8 mg, 2.35 mmol) and Et$_4$NF·$x$H$_2$O (980.6 mg, 6.56 mmol anhydrous) were added to a flask with a stir bar propylene carbonate (1.0 mL). As Et$_4$NF·$x$H$_2$O cannot be dried without decomposition, the exact level of hydration is unknown and an excess is used. This mixture is heated to 80 °C and allowed to stir until complete dissolution of the CeF$_4$ occurs. After cooling to room temperature, acetone (10 mL) followed by Et$_2$O (20 mL) are added to precipitate $(Et_4N)_2CeF_6$·6H$_2$O. This colorless solid was redissolved in a solution of Ph$_4$PCl (1865.9 mg, 4.99 mmol) in MeCN (15.0 mL). Et$_2$O (20 mL) is added, and the solution is stirred for 5 min, during which a colorless precipitate formed. The solvent was decanted and the solid washed three times with acetone (20 mL). The resulting solids were dried overnight under vacuum to remove volatile materials before being brought into a glovebox. The solid was dissolved in MeCN (20 mL), and Et$_2$O was allowed to vapor diffuse into the solution overnight. X-ray quality crystals were produced in 79.5% yield with respect to the starting CeF$_4$. Higher yields may be obtained by allowing the vapor diffusion to run for a longer time, with a maximum yield after 1 week. This crystallization afforded off-white chunks of $(Ph_4P)_2CeF_6$·MeCN (CCDC: 2359877). The solvent of crystallization can be removed by drying in vacuo. IR (KBr, cm$^{-1}$): 438.7 (m), 529.2 (m), 615.0 (w), 691.7 (m), 723.7 (m), 763.0 (m), 801.0 (w), 996.2 (w), 1025.0 (w), 1106.6 (m), 1165.8 (w), 1189.6 (w), 1261.9 (w), 1312.1 (w), 1340.2 (w), 1377.5 (m), 1440.5 (m), 1463.6 (s), 1583.5 (w), 1632.6 (w), 1658.1 (w), 1680.1 (w), 2672.9 (w), 2725.8 (w), 2855.1 (s), 2924.7 (s), 2957.3 (s), 3198.4 (w), 3295.7 (w), 3429.6 (w), 3514.3 (w), 3661.3 (w). Raman (532 nm): 528 cm$^{-1}$. $^{19}$F NMR (CD$_3$CN): 180.7 ppm externally referenced against CFCl$_3$. Anal. Calcd for C$_{48}$H$_{40}$P$_2$CeF$_6$: C, 61.80%; H, 4.32%. Found: C, 61.56%; H, 4.44%.

**STXM Sample Preparation.** Glassware and sample windows were stored in an oven at 160 °C for at least 12 h prior to use. Organic solvents were purified by passage through a column of activated alumina prior to use. A small amount (~1 mg) of each

sample was dissolved in 1 mL of MeCN, and a pipet was used to transfer a small aliquot of this solution onto a $Si_3N_4$ window (100 nm, Silson). The MeCN was allowed to evaporate and deposit crystallites of the sample onto the window. After drying for a few more minutes, a second window was placed over the sample, and the edges were sealed with Hardman Double/Bubble epoxy. This preparation results in the samples being sealed off from environmental oxygen and moisture while being transferred into the instrument chamber for measurement.

**Fluorine K-Edge and Cerium $M_{4,5}$-Edge XAS STXM Measurements.** Fluorine K-edge spectra, Ce $M_{4,5}$-edge spectra, and elemental maps were taken using the STXM instrument at the Canadian Light Source Spectromicroscopy (SM) beamline (10ID-1) in a vacuum chamber at ambient temperature. An energy calibration was performed at the F K-edge using $SF_6$ gas (688.0 eV) for F and Ne gas (867.12 eV) for Ce. The X-ray beam was focused onto the sample with a zone plate, and the X-ray transmission was detected. The spot size and spectral resolution were determined from characteristics of the 35 nm zone plate. Single-energy images were collected by raster-scanning the sample with monochromatic light and recording the transmitted intensity as a function of sample position. A collection of these monochromatic images taken at multiple, closely spaced photon energies across the absorption edge form a "stack." The transmittance data were converted to optical density using the Beer–Lambert law. Incident beam intensity was measured through the sample-free region of the $Si_3N_4$ window. Spectra were obtained by averaging over the signal of the sample deposited on the window. During the experiment, the samples showed no signs of radiation damage, and the spectra were reproducible with multiple independent crystallites.

**Fluorine K-Edge XAS Data Reduction.** The normalization was completed based on a previously described procedure. For each scan, the pre-edge region was fit to a Victoreen polynomial, and that polynomial was extrapolated across the energy range measured. This extrapolated polynomial curve is then subtracted from the experimental data. To normalize the spectral intensity, a third-order polynomial is fit to the postedge region in this background-subtracted spectrum. Then, this spectrum is divided by a constant so that the intensity at the postedge normalization energy (714 eV) in the fit is equal to one. Once this normalization process is complete for each scan, the normalized spectra are averaged to produce the final, normalized spectrum. The spectral intensities of the pre-edge transitions were determined by fitting the spectrum with symmetrically constrained Gaussian functions to represent pre-edge features and a step function with a 1:1 ratio of arctangent and error function contributions to represent the rising edge. Spectral curve fitting was performed using a modified version of the EDG_FIT procedure in IGOR Pro 8.0.[101] The pre-edge peak intensities are determined from the area under the functions used to fit them. Uncertainty in the areas under the Gaussian functions due to background subtraction, normalization, and spectral curve fitting is estimated at 10% or less based on previous studies,[34] curve fitting error, and STXM data reproducibility.

**Ce $L_3$-Edge XAS Sample Preparation and Measurement.** X-ray absorption near edge structure data at the Ce $L_3$ absorption edge were collected at the Stanford Synchrotron Radiation Lightsource (SSRL) beamline 11-2 using a Si(220) ($\varphi = 0°$) monochromator detuned to 50% and a Rh-coated harmonic rejection mirror with a cutoff energy set near 10 keV. The vertical slit height was sufficiently narrow that the energy resolution was core–hole lifetime limited. Data were collected in transmission geometry and the monochromator energy was calibrated by defining the energy of the first inflection point at the Ce $L_3$-edge of the absorption from a $CeO_2$ standard to be 5724.0 eV. Data were processed by subtracting a Chebychev spline pre-edge background and normalizing the edge step to one. Powder samples were prepared in an argon-filled glovebox for measurement by mixing with dry boron nitride and packed into a slotted aluminum holder with aluminized mylar windows, sealed with crushed indium wire. Since the samples are air sensitive, the sealed holders were kept under argon until measurement, and exposed to air for less than 1 min during transfer to vacuum. Samples were measured both at 50 and

300 K using a liquid-helium cooled cryostat to test for temperature dependence of the resulting spectra. An easily oxidizable "canary" sample, such as cerium tris(tetramethylcyclopentadienyl) ($CeCp_3^{tet}$), was measured along with the samples to ensure that no $O_2$ had leaked into the sample holder during measurement.

Fitting of the spectra was performed using the FITEDGE utility, a component of the RSXAP software library.[102] For each spectrum, 5 peaks comprised of 50% each equal-width Gaussian and Lorentzian components (commonly termed a pseudo-Voigt) were used to model resonant transitions in the edge. The edge step was modeled as a pure error function (i.e., integrated Gaussian) with a half-width ($\sigma$) of about twice the core-hole lifetime broadening ($\Gamma$) for the Ce $L_3$-edge ($\Gamma = 3.27$ eV). This larger width models the chemical broadening of the continuum excitations, which XPS suggest should have a double structure similar to those of the bound resonances of the edge.[103] Due to strong correlation between the crystal field subpeaks of the $f^1$ and $f^0$ multiplets, errors in the area have been estimated using a profiling method, rather than the typical treatment based on the diagonal elements of the covariance matrix implemented in FITEDGE. In order to make accurate comparisons to the present data, curve fits to the Ce $L_3$-edge data reported previously for $(Et_4N)_2CeCl_6$[2] and $Ce(PN^*)_4$[6] were modified with a broad edge step whose position and width are constrained by the edge features.

**SQUID Magnetometry.** Samples of $(Ph_4P)_2CeF_6$ (8.6 mg) and $(Et_4N)_2CeCl_6$ (11.8 mg) were loaded into 3 mm (O.D.) quartz tubes and sandwiched between two pieces of quartz wool (QW) by a modified literature procedure.[47−49] Outside the glovebox, a preweighed amount of quartz wool (($Ph_4P)_2CeF_6$, QW = 3.6 mg; $(Et_4N)_2CeCl_6$, QW = 4.2 mg), which had previously been leeched with oxalic and hydrochloric acid, was inserted and packed into a quartz tube with quartz rods. Afterward, the tubes were oven-dried for 24 h at 150 °C. Inside a glovebox, crystals of both complexes were ground in oven-dried agate mortars and pestles and two 0.075" (O.D.) polyimide liners were placed inside both ends of a quartz tube. A mild vacuum was applied to one end, such that no quartz wool was pushed out; the other end was used to vacuum sample into the tube landing onto the quartz wool without touching the sidewalls. The polyimide liners were removed, and a second piece of quartz wool was inserted into the tube on top of the compound. The sample was compressed into a pellet with two quartz rods. The ends of the tube were capped with two 5 mm NMR tube rubber septa. The center of the tube was wrapped with a piece of open-cell foam, saturated with liquid nitrogen, and the ends were flame-sealed with a propane/oxygen torch. Variable temperature magnetization data were recorded from 3 to 400 K at 1 and 5 T with a 7 T Quantum Design MPMS magnetometer utilizing a superconducting quantum interference device (SQUID). Molar susceptibility, $\chi_m$, was calculated using the formula

$$\chi_m = \frac{MW}{m}\left[\frac{M_{meas} - M_{imp}}{H} - \chi_{QW}\right] - \chi_d$$

In this formula, MW is the molecular weight of the sample, $m$ is the mass of the sample, $M_{meas}$ is the measured magnetization, $M_{imp}$ is the magnetization due to an assumed ferromagnetic impurity, $H$ is the applied field, and $\chi_{QW}$ as well as $\chi_d$ are the diamagnetic corrections due to the quartz wool and the sample, respectively, calculated from Pascal's constants.[51] The different applied fields were chosen to saturate $M_{imp}$ so that its field dependence could be treated as a constant. The value of $M_{imp}$ was allowed to vary to minimize the least-squares difference of $\chi_m T$ between the measured fields from 100 to 300 K.

**Ce $M_{4,5}$-Edge CTM Calculation Parameters.** The CTM calculations on the Ce $M_{4,5}$-edge of $CeF_6^{2−}$ were performed using the Theo Thole multiplet code, with modifications by Ogasawara, as maintained and used by the CTM4XAS program.[79] The CTM4XAS graphical user interface does not support charge transfer calculations for the lanthanide $M_{4,5}$-edges, so the calculations must be run from the command line in the underlying CTM code. This calculation was performed in analogy to a previous calculation on $CeCl_6^{2−}$.[2] The

atomic parameters were kept the same, except for the spin−orbit coupling, which was reduced to 98% (versus 99% with $CeCl_6^{2-}$). For the charge transfer component of the calculation, the hopping integrals in the ground and final states, $T_{gs}$ and $T_{fs}$, were both set to 0.92 eV. The ground state charge transfer energy, $\Delta E_{gs}$, was set to 4.6 eV, and the final state charge transfer energy, $\Delta E_{fs}$, was set to 1.8 eV. Lorentzian broadenings of 0.4 and 0.6 eV were applied to the $M_5$ and $M_4$-edges, respectively, and Gaussian broadening of 0.25 eV was applied to both edges. The calculated spectrum was shifted by −0.15 eV to match the experimental energies. The complete set of input and output files is given in the Supporting Information.

**Ground State Electronic Structure Calculations.** Starting from the crystal structures, equilibrium structures of octahedral $CeL_6^{2-}$ (L = F, Cl) complexes were optimized with Kohn−Sham DFT with the ORCA program (version 5.0.3).[104,105] The popular B3LYP hybrid generalized gradient approximation[106] was used, in conjunction with all-electron ANO-RCC-QZP basis sets[107,108] for all atoms and the scalar-relativistic, second-order Douglas−Kroll−Hess (DKH2) Hamiltonian.[109] Additional B3LYP single-point energy calculations were performed on $O_h$ structures of the complexes with the metal−ligand bond lengths fixed to the averaged distances in the crystal structures. Geometry optimizations were additionally performed with coupled cluster theory with singles, doubles and perturbative triples [CCSD-(T)],[110] within the domain-based local pair natural orbital (DLPNO) formalism,[111,112] by varying the Ce−L bond lengths in the octahedral complexes in increments of 0.01 Å. The resolution of identity approximation for the Coulomb and exchange terms (RIJK) was applied, together with large automatically generated auxiliary basis sets (AUTOAUX).[113] Single-point energy calculations with orbital-optimized coupled cluster doubles OO-CCD[114,115] were additionally performed on the "averaged" crystal structures with Ce−F and Ce−Cl bond lengths of 2.152 and 2.599 Å, respectively. Heterolytic bond dissociation energies (BDEs) were also calculated to assess the polarity of the Ce−L bonds. Counterpoise corrections were not applied because of the high quality of the basis sets used. Reported atomic shell populations and atomic charges based on the Mulliken partitioning were checked against results from natural population analyses with the NBO program,[116] showing similar trends. Comments on the optimized geometries, (localized) MOs and BDEs are given in the Supporting Information file.

**Ab Initio Calculation of the Ce $L_3$-Edge and F and Cl K-Edge XAS.** The crystal structures (averaged bond lengths) of $CeF_6^{2-}$ and $CeCl_6^{2-}$ were subjected to WFT calculations for determining the ligand K-edge and Ce $L_3$-edge X-ray absorption structure (XAS) spectra. These calculations were performed with OpenMolcas.[117] Following previous work on ab initio XAS,[32,66,67] we performed a series of RAS-SCF[118] calculations for the valence and the core excited states targeted in the XAS experiments. For the ligand K edges, the 6 ligand 1s orbitals with 12 electrons comprised RAS1 and the unoccupied, antibonding MOs with Ce(5f)−L(np) and Ce(5d)−L(np) character ($t_{1u}$, $t_{2u}$, $e_g$, and $t_{2g}$) comprised RAS2. These K-edge calculations were started from B3LYP orbitals. A similar strategy was employed in ref 58 for calculating the Cl K-edge spectrum of $CeCl_6^{2-}$ using a relativistic, variational multireference configuration interaction approach (MRCI). Despite using a somewhat less demanding correlation method in the present study, PT2 vs MRCI in ref 58, the calculated spectra are in excellent agreement. Concerning the Ce $L_3$-edges, since Ce(4f)−L(np) covalency appears to various extents in both the $t_{1u}$ and $t_{2u}$ irreps, two sets of calculations were performed to obtain the total intensity, both using the Ce $2p^6$ core for RAS1 and the unoccupied $t_{2g}$ and $e_g$ MOs with Ce(5d) character in RAS3. In a first set of calculations, the $t_{1u}$ Ce(4f)−L(np) bonding and antibonding MOs with six electrons comprised RAS2 whereas, in a second set of calculations, RAS2 corresponded to the $t_{2u}$ Ce(4f)−L(np) bonding and antibonding MOs and six electrons. Performing these two sets of calculations was necessary to allow Ce(III) and Ce(IV) configurations, generated via covalency in both the $t_{1u}$ and $t_{2u}$ irreps, to contribute to the initial and final states that generate intensity under the $L_3$-edges. In all these calculations targeting the Ce $L_3$-edge, the ground state wave function was obtained from a state-

average calculation over the four lowest energy valence states of $A_g$ symmetry ($D_{2h}$ point group). Concerning the core excited state wave functions, these were obtained in state-average calculations of all possible such states in the electric dipole-allowed irreps of $D_{2h}$, i.e., $b_{1u}$, $b_{2u}$, and $b_{3u}$. Using the RAS-SCF wave functions, dynamic correlation was introduced in the state energies via RAS perturbation theory at second-order (PT2).[119,120] The oscillator strengths necessary for generating intensities between the ground state and the core excited states were calculated with the RAS-SCF wave functions and RAS-PT2 energies with the RAS state-interaction (RASSI) module of OpenMolcas. For the Ce $L_3$-edge, the ratio of the scaling factors used for the chloride vs the fluoride complex was 1.78, reflecting that the calculations produced an overall stronger intensity at the Ce $L_3$-edge for $CeF_6^{2-}$ compared to $CeCl_6^{2-}$, in agreement with the experimental trend. All XAS calculations used a finite-volume Gaussian representation of the nuclear charges. Modified ANO-RCC-VTZP basis sets were used in these XAS calculations. Following a previous strategy,[84] the two most diffuse Ce d-type functions (exponents of 0.080 and 0.032) and ligand p-type functions (exponents of 0.155 and 0.054 for F, 0.103 and 0.041 for Cl) were removed from the basis sets in order to obtain a better description of the virtual MOs, in particular those of $e_g$ symmetry.

## ■ ASSOCIATED CONTENT

**Ⓢ Supporting Information**

The Supporting Information is available free of charge at https://pubs.acs.org/doi/10.1021/jacs.4c07459.

> Complete fit parameters, additional computational details, additional data interpretation details, crystallographic information, Raman, IR, UV−vis, CV, and tables of X-ray absorption data (PDF)

**Accession Codes**

CCDC 2359877 contains the supplementary crystallographic data for this paper. These data can be obtained free of charge via www.ccdc.cam.ac.uk/data_request/cif, or by emailing data_request@ccdc.cam.ac.uk, or by contacting The Cambridge Crystallographic Data Centre, 12 Union Road, Cambridge CB2 1EZ, UK; fax: +44 1223 336033.

## ■ AUTHOR INFORMATION

**Corresponding Authors**

**Jochen Autschbach** − *Department of Chemistry, University at Buffalo, State University of New York, Buffalo, New York 14260, United States;* ⓞ orcid.org/0000-0001-9392-877X; Email: jochena@buffalo.edu

**Stefan G. Minasian** − *Chemical Sciences Division, Lawrence Berkeley National Laboratory, Berkeley, California 94720, United States;* ⓞ orcid.org/0000-0003-1346-7497; Email: sgminasian@lbl.gov

**Authors**

**Jacob A. Branson** − *Department of Chemistry, University of California, Berkeley, Berkeley, California 94720, United States; Chemical Sciences Division, Lawrence Berkeley National Laboratory, Berkeley, California 94720, United States;* ⓞ orcid.org/0000-0002-3523-0303

**Patrick W. Smith** − *Chemical Sciences Division, Lawrence Berkeley National Laboratory, Berkeley, California 94720, United States;* ⓞ orcid.org/0000-0001-5575-4895

**Dumitru-Claudiu Sergentu** − *RA-03 (RECENT AIR) Laboratory and Faculty of Chemistry, Alexandru Ioan Cuza University of Iași, Iași 700506, Romania;* ⓞ orcid.org/0000-0001-6570-5245

**Dominic R. Russo** − *Department of Chemistry, University of California, Berkeley, Berkeley, California 94720, United States; Chemical Sciences Division, Lawrence Berkeley National Laboratory, Berkeley, California 94720, United States;* ⊙ orcid.org/0000-0003-4014-9216

**Himanshu Gupta** − *P. Roy and Diana T. Vagelos Laboratories, Department of Chemistry, University of Pennsylvania, Philadelphia, Pennsylvania 19104, United States;* ⊙ orcid.org/0000-0001-9843-3020

**Corwin H. Booth** − *Chemical Sciences Division, Lawrence Berkeley National Laboratory, Berkeley, California 94720, United States*

**John Arnold** − *Department of Chemistry, University of California, Berkeley, Berkeley, California 94720, United States; Chemical Sciences Division, Lawrence Berkeley National Laboratory, Berkeley, California 94720, United States;* ⊙ orcid.org/0000-0001-9671-227X

**Eric J. Schelter** − *P. Roy and Diana T. Vagelos Laboratories, Department of Chemistry, University of Pennsylvania, Philadelphia, Pennsylvania 19104, United States;* ⊙ orcid.org/0000-0002-8143-6206

Complete contact information is available at:
https://pubs.acs.org/10.1021/jacs.4c07459

**Notes**
The authors declare no competing financial interest.

## ■ ACKNOWLEDGMENTS

## ■ REFERENCES

(1) Altman, A. B.; Pacold, J. I.; Wang, J.; Lukens, W. W.; Minasian, S. G. Evidence for 5d-σ and 5d-π Covalency in Lanthanide Sesquioxides from Oxygen K-Edge X-Ray Absorption Spectroscopy. *Dalton Trans.* **2016**, *45* (24), 9948−9961.

(2) Löble, M. W.; Keith, J. M.; Altman, A. B.; Stieber, S. C. E.; Batista, E. R.; Boland, K. S.; Conradson, S. D.; Clark, D. L.; Lezama Pacheco, J.; Kozimor, S. A.; Martin, R. L.; Minasian, S. G.; Olson, A. C.; Scott, B. L.; Shuh, D. K.; Tyliszczak, T.; Wilkerson, M. P.; Zehnder, R. A. Covalency in Lanthanides. An X-Ray Absorption Spectroscopy and Density Functional Theory Study of LnCl₆ˣ − (x = 3, 2). *J. Am. Chem. Soc.* **2015**, *137* (7), 2506−2523.

(3) Kaltsoyannis, N.; Scott, P. *The F-Elements*; Oxford University Press: Oxford, 1999.

(4) Burns, C. J.; Bursten, B. E. Covalency in F-Element Organometallic Complexes: Theory and Experiment. *Comments Inorg. Chem.* **1989**, *9* (2), 61−93.

(5) Qiao, Y.; Yin, H.; Moreau, L. M.; Feng, R.; Higgins, R. F.; Manor, B. C.; Carroll, P. J.; Booth, C. H.; Autschbach, J.; Schelter, E. J. Cerium(IV) Complexes with Guanidinate Ligands: Intense Colors and Anomalous Electronic Structures. *Chem. Sci.* **2021**, *12* (10), 3558−3567.

(6) Rice, N. T.; Su, J.; Gompa, T. P.; Russo, D. R.; Telser, J.; Palatinus, L.; Bacsa, J.; Yang, P.; Batista, E. R.; La Pierre, H. S. Homoleptic Imidophosphorane Stabilization of Tetravalent Cerium. *Inorg. Chem.* **2019**, *58* (8), 5289−5304.

(7) Cheisson, T.; Kersey, K. D.; Mahieu, N.; McSkimming, A.; Gau, M. R.; Carroll, P. J.; Schelter, E. J. Multiple Bonding in Lanthanides and Actinides: Direct Comparison of Covalency in Thorium(IV)- and Cerium(IV)-Imido Complexes. *J. Am. Chem. Soc.* **2019**, *141* (23), 9185−9190.

(8) Gregson, M.; Lu, E.; McMaster, J.; Lewis, W.; Blake, A. J.; Liddle, S. T. A Cerium(IV)−Carbon Multiple Bond. *Angew. Chem., Int. Ed.* **2013**, *52* (49), 13016−13019.

(9) So, Y.-M.; Wang, G.-C.; Li, Y.; Sung, H. H.-Y.; Williams, I. D.; Lin, Z.; Leung, W.-H. A Tetravalent Cerium Complex Containing a Ce = O Bond. *Angew. Chem., Int. Ed.* **2014**, *53* (6), 1626−1629.

(10) Solola, L. A.; Zabula, A. V.; Dorfner, W. L.; Manor, B. C.; Carroll, P. J.; Schelter, E. J. Cerium(IV) Imido Complexes: Structural, Computational, and Reactivity Studies. *J. Am. Chem. Soc.* **2017**, *139* (6), 2435−2442.

(11) Kynman, A. E.; Elghanayan, L. K.; Desnoyer, A. N.; Yang, Y.; Sévery, L.; Di Giuseppe, A.; Tilley, T. D.; Maron, L.; Arnold, P. L. Controlled Monodefluorination and Alkylation of C(Sp³)−F Bonds by Lanthanide Photocatalysts: Importance of Metal−Ligand Cooperativity. *Chem. Sci.* **2022**, *13* (47), 14090−14100.

(12) Yang, Q.; Wang, Y.-H.; Qiao, Y.; Gau, M.; Carroll, P. J.; Walsh, P. J.; Schelter, E. J. Photocatalytic C−H Activation and the Subtle Role of Chlorine Radical Complexation in Reactivity. *Science* **2021**, *372* (6544), 847−852.

(13) Yin, H.; Jin, Y.; Hertzog, J. E.; Mullane, K. C.; Carroll, P. J.; Manor, B. C.; Anna, J. M.; Schelter, E. J. The Hexachlorocerate(III) Anion: A Potent, Benchtop Stable, and Readily Available Ultraviolet A Photosensitizer for Aryl Chlorides. *J. Am. Chem. Soc.* **2016**, *138* (50), 16266−16273.

(14) Yin, H.; Carroll, P. J.; Anna, J. M.; Schelter, E. J. Luminescent Ce(III) Complexes as Stoichiometric and Catalytic Photoreductants for Halogen Atom Abstraction Reactions. *J. Am. Chem. Soc.* **2015**, *137* (29), 9234−9237.

(15) Qiao, Y.; Schelter, E. J. Lanthanide Photocatalysis. *Acc. Chem. Res.* **2018**, *51* (11), 2926−2936.

(16) Nagata, T.; Miyajima, K.; Hardy, R. A.; Metha, G. F.; Mafuné, F. Reactivity of Oxygen Deficient Cerium Oxide Clusters with Small Gaseous Molecules. *J. Phys. Chem. A* **2015**, *119* (22), 5545−5552.

(17) Fokin, A. A.; Peleshanko, S. A.; Gunchenko, P. A.; Gusev, D. V.; Schreiner, P. R. Hydrocarbon Activation with Cerium(IV) Ammonium Nitrate: Free Radical versus Oxidative Pathways. *Eur. J. Org Chem.* **2000**, *2000* (19), 3357−3362.

(18) Pham, H.-L.; Rajeshkumar, T.; Wang, L. U.; Ng, Y. H.; Wong, K.-H.; So, Y.-M.; Sung, H. H. Y.; Lortz, R.; Williams, I. D.; Maron, L.; Leung, W.-H. Synthesis and Reactivity of Redox-Active Cerium(IV) Aryloxide Complexes. *Organometallics* **2023**, *42*, 1094−1105.

(19) Wong, W.-H.; Wong, K.-H.; Au-Yeung, K.-C.; So, Y.-M.; Cheung, W.-M.; Sung, H. H. Y.; Williams, I. D.; Leung, W.-H. Synthesis, Structure, and Reactivity of Tetravalent Cerium Complexes Containing Oxidizing Oxyanion Ligands. *J. Organomet. Chem.* **2019**, *899*, 120902.

(20) Qasim, H. M.; Ayass, W. W.; Donfack, P.; Mougharbel, A. S.; Bhattacharya, S.; Nisar, T.; Balster, T.; Solé-Daura, A.; Römer, I.; Goura, J.; Materny, A.; Wagner, V.; Poblet, J. M.; Bassil, B. S.; Kortz, U. Peroxo-Cerium(IV)-Containing Polyoxometalates: $[Ce^{IV}_6(O_2)_9(GeW_{10}O_{37})_3]^{24-}$, a Recyclable Homogeneous Oxidation Catalyst. *Inorg. Chem.* **2019**, *58* (17), 11300−11307.

(21) Matthias, B. T.; Suhl, H.; Corenzwit, E. Ferromagnetic Superconductors. *Phys. Rev. Lett.* **1958**, *1* (12), 449−450.

(22) Andres, K.; Graebner, J. E.; Ott, H. R. 4f-Virtual-Bound-State Formation in CeAl$_3$ at Low Temperatures. *Phys. Rev. Lett.* **1975**, *35* (26), 1779−1782.

(23) Kaindl, G.; Kalkowski, G.; Brewer, W. D.; Sampathkumaran, E. V.; Holtzberg, F.; v Wittenau, A. S. 4f Occupation and Hybridization from M-Shell Excitations in Rare-Earth Materials. *J. Magn. Magn. Mater.* **1985**, *47−48*, 181−189.

(24) Amorese, A.; Hansmann, P.; Marino, A.; Körner, P.; Willers, T.; Walters, A.; Zhou, K.-J.; Kummer, K.; Brookes, N. B.; Lin, H.-J.; Chen, C.-T.; Lejay, P.; Haverkort, M. W.; Tjeng, L. H.; Severing, A. Orbital Selective Coupling in CeRh$_3$B$_2$: Coexistence of High Curie and High Kondo Temperatures. *Phys. Rev. B* **2023**, *107* (11), 115164.

(25) Matar, S. F. Review on Cerium Intermetallic Compounds: A Bird's Eye Outlook through DFT. *Prog. Solid State Chem.* **2013**, *41* (3), 55−85.

(26) Humphries, M. *Rare Earth Elements: The Global Supply Chain*; Congressional Research Service: Washington, D.C., 2013; p R41347.

(27) Bianconi, A.; Marcelli, A.; Dexpert, H.; Karnatak, R.; Kotani, A.; Jo, T.; Petiau, J. Specific Intermediate-Valence State of Insulating 4f Compounds Detected by L$_3$ x-Ray Absorption. *Phys. Rev. B: Condens. Matter Mater. Phys.* **1987**, *35* (2), 806−812.

(28) Dexpert, H.; Karnatak, R. C.; Esteva, J.-M.; Connerade, J. P.; Gasgnier, M.; Caro, P. E.; Albert, L. X-Ray Absorption Studies of CeO$_2$, PrO$_2$, and TbO$_2$. II. Rare-Earth Valence State by L$_{III}$ Absorption Edges. *Phys. Rev. B: Condens. Matter Mater. Phys.* **1987**, *36* (3), 1750−1753.

(29) Kaindl, G.; Schmiester, G.; Sampathkumaran, E. V.; Wachter, P. Pressure-Induced Changes in L$_{III}$ x-Ray-Absorption near-Edge Structure of CeO$_2$ and CeF$_4$: Relevance to 4f-Electronic Structure. *Phys. Rev. B: Condens. Matter Mater. Phys.* **1988**, *38* (14), 10174−10177.

(30) Kotani, A.; Kvashnina, K. O.; Butorin, S. M.; Glatzel, P. A New Method of Directly Determining the Core−Hole Effect in the Ce L$_3$ XAS of Mixed Valence Ce Compounds—An Application of Resonant X-Ray Emission Spectroscopy. *J. Electron Spectrosc. Relat. Phenom.* **2011**, *184* (3−6), 210−215.

(31) Duignan, T. J.; Autschbach, J. Impact of the Kohn−Sham Delocalization Error on the 4f Shell Localization and Population in Lanthanide Complexes. *J. Chem. Theory Comput.* **2016**, *12* (7), 3109−3121.

(32) Sergentu, D.; Booth, C. H.; Autschbach, J. Probing Multi-configurational States by Spectroscopy: The Cerium XAS L$_3$-edge Puzzle. *Chem.—Eur. J.* **2021**, *27* (25), 7239−7251.

(33) Glaser, T.; Hedman, B.; Hodgson, K. O.; Solomon, E. I. Ligand K-Edge X-Ray Absorption Spectroscopy: A Direct Probe of Ligand−Metal Covalency. *Acc. Chem. Res.* **2000**, *33* (12), 859−868.

(34) Solomon, E. I.; Hedman, B.; Hodgson, K. O.; Dey, A.; Szilagyi, R. K. Ligand K-Edge X-Ray Absorption Spectroscopy: Covalency of Ligand−Metal Bonds. *Coord. Chem. Rev.* **2005**, *249* (1−2), 97−129.

(35) Hedman, B.; Hodgson, K. O.; Solomon, E. I. X-Ray Absorption Edge Spectroscopy of Ligands Bound to Open-Shell Metal Ions: Chlorine K-Edge Studies of Covalency in CuCl$_4$$^{2-}$. *J. Am. Chem. Soc.* **1990**, *112* (4), 1643−1645.

(36) Neese, F.; Hedman, B.; Hodgson, K. O.; Solomon, E. I. Relationship between the Dipole Strength of Ligand Pre-Edge Transitions and Metal−Ligand Covalency. *Inorg. Chem.* **1999**, *38* (21), 4854−4860.

(37) Shadle, S. E.; Hedman, B.; Hodgson, K. O.; Solomon, E. I. Ligand K-Edge x-Ray Absorption Spectroscopic Studies: Metal-Ligand Covalency in a Series of Transition Metal Tetrachlorides. *J. Am. Chem. Soc.* **1995**, *117* (8), 2259−2272.

(38) Albright, T.; Burdett, J.; Whangbo, M.-H. *Orbital Interactions in Chemistry*; John Wiley & Sons, 2013.

(39) Whangbo, M.-H.; Schlegel, H. B.; Wolfe, S. Molecular Orbitals from Group Orbitals. 3. Quantitative Perturbational Molecular Orbital Analysis of Ab Initio SCF-MO Wave Functions. *J. Am. Chem. Soc.* **1977**, *99* (5), 1296−1304.

(40) Burdett, J. K. The .sigma. strength of ligands coordinated to transition metal ions. *J. Am. Chem. Soc.* **1979**, *101* (3), 580−583.

(41) Hoffmann, R. Interaction of Orbitals through Space and through Bonds. *Acc. Chem. Res.* **1971**, *4* (1), 1−9.

(42) Balasekaran, S. M.; Hagenbach, A.; Lentz, D.; Poineau, F. Tetraethylammonium Hexafluoro Uranate(IV), Hafnate(IV), and Cerate(IV) Salts: Preparation and Solid-state Structure. *Z. Anorg. Allg. Chem.* **2019**, *645* (16), 1052−1056.

(43) Forrest, I. W.; Lane, A. P. Single-Crystal Polarized Infrared and Raman Spectra and Normal-Coordinate Analysis of Some Group 4 Complex Hexafluorometalates. *Inorg. Chem.* **1976**, *15* (2), 265−269.

(44) Brown, T. L.; McDugle, W. G.; Kent, L. G. Vibrational and Pure Nuclear Quadrupole Resonance Spectra of Hexahalometalates. *J. Am. Chem. Soc.* **1970**, *92* (12), 3645−3653.

(45) Nakamoto, K. *Infrared and Raman Spectra of Inorganic and Coordination Compounds: Part A: Theory and Applications in Inorganic Chemistry*; John Wiley & Sons, Inc., 2009.

(46) Adams, D. M.; Morris, D. M. Vibrational Spectra of Halides and Complex Halides. Part IV. Some Tetrahalogenothallates and the Effects of d-Electronic Structure on the Frequencies of Hexachlorometallates. *J. Chem. Soc. A* **1968**, 694−695.

(47) Booth, C. H.; Kazhdan, D.; Werkema, E. L.; Walter, M. D.; Lukens, W. W.; Bauer, E. D.; Hu, Y.-J.; Maron, L.; Eisenstein, O.; Head-Gordon, M.; Andersen, R. A. Intermediate-Valence Tautomerism in Decamethylytterbocene Complexes of Methyl-Substituted Bipyridines. *J. Am. Chem. Soc.* **2010**, *132* (49), 17537−17549.

(48) Booth, C. H.; Walter, M. D.; Kazhdan, D.; Hu, Y.-J.; Lukens, W. W.; Bauer, E. D.; Maron, L.; Eisenstein, O.; Andersen, R. A. Decamethylytterbocene Complexes of Bipyridines and Diazabutadienes: Multiconfigurational Ground States and Open-Shell Singlet Formation. *J. Am. Chem. Soc.* **2009**, *131* (18), 6480−6491.

(49) Walter, M. D.; Booth, C. H.; Lukens, W. W.; Andersen, R. A. Cerocene Revisited: The Electronic Structure of and Interconversion Between Ce$_2$(C$_8$H$_8$)$_3$ and Ce(C$_8$H$_8$)$_2$. *Organometallics* **2009**, *28* (3), 698−707.

(50) Walter, M. D.; Schultz, M.; Andersen, R. A. Weak Paramagnetism in Compounds of the Type Cp′$_2$Yb(Bipy). *New J. Chem.* **2006**, *30* (2), 238−246.

(51) Bain, G. A.; Berry, J. F. Diamagnetic Corrections and Pascal's Constants. *J. Chem. Educ.* **2008**, *85* (4), 532.

(52) Myers, A. J.; Tarlton, M. L.; Kelley, S. P.; Lukens, W. W.; Walensky, J. R. Synthesis and Utility of Neptunium(III) Hydrocarbyl Complex. *Angew. Chem., Int. Ed.* **2019**, *58* (42), 14891−14895.

(53) Moreau, L. M.; Lapsheva, E.; Amaro-Estrada, J. I.; Gau, M. R.; Carroll, P. J.; Manor, B. C.; Qiao, Y.; Yang, Q.; Lukens, W. W.; Sokaras, D.; Schelter, E. J.; Maron, L.; Booth, C. H. Electronic Structure Studies Reveal 4f/5d Mixing and Its Effect on Bonding Characteristics in Ce-Imido and -Oxo Complexes. *Chem. Sci.* **2022**, *13* (6), 1759−1773.

(54) Booth, C. H.; Walter, M. D.; Daniel, M.; Lukens, W. W.; Andersen, R. A. Self-Contained Kondo Effect in Single Molecules. *Phys. Rev. Lett.* **2005**, *95* (26), 267202.

(55) Halbach, R. L.; Nocton, G.; Booth, C. H.; Maron, L.; Andersen, R. A. Cerium Tetrakis(Tropolonate) and Cerium Tetrakis-(Acetylacetonate) Are Not Diamagnetic but Temperature-Independent Paramagnets. *Inorg. Chem.* **2018**, *57* (12), 7290−7298.

(56) Van Vleck, J. H. *The Theory of Electric and Magnetic Susceptibilities*; Clarendon Press, 1932.

(57) Balazs, G.; Cloke, F. G. N.; Green, J. C.; Harker, R. M.; Harrison, A.; Hitchcock, P. B.; Jardine, C. N.; Walton, R. Cerium(III) and Cerium(IV) Bis($\eta^8$-Pentalene) Sandwich Complexes: Synthetic, Structural, Spectroscopic, and Theoretical Studies. *Organometallics* **2007**, *26* (13), 3111−3119.

(58) Shumilov, K. D.; Jenkins, A. J.; La Pierre, H. S.; Vlaisavljevich, B.; Li, X. Overdestabilization vs Overstabilization in the Theoretical Analysis of F-Orbital Covalency. *J. Am. Chem. Soc.* **2024**, *146* (17), 12030−12039.

(59) Wuilloud, E.; Delley, B.; Schneider, W.-D.; Baer, Y. Spectroscopic Evidence for Localized and Extended f-Symmetry States in $CeO_2$. *Phys. Rev. Lett.* **1984**, *53* (2), 202−205.

(60) Mooßen, O.; Dolg, M. Two Interpretations of the Cerocene Electronic Ground State. *Chem. Phys. Lett.* **2014**, *594*, 47−50.

(61) Ashley, A.; Balazs, G.; Cowley, A.; Green, J.; Booth, C. H.; O'Hare, D. Bis(Permethylpentalene)Cerium − Another Ambiguity in Lanthanide Oxidation State. *Chem. Commun.* **2007**, 1515−1517.

(62) Minasian, S. G.; Batista, E. R.; Booth, C. H.; Clark, D. L.; Keith, J. M.; Kozimor, S. A.; Lukens, W. W.; Martin, R. L.; Shuh, D. K.; Stieber, S. C. E.; Tyliszczak, T.; Wen, X. Quantitative Evidence for Lanthanide-Oxygen Orbital Mixing in $CeO_2$, $PrO_2$, and $TbO_2$. *J. Am. Chem. Soc.* **2017**, *139* (49), 18052−18064.

(63) Kotani, A. Core-hole Effect in the Ce $L_3$ X-ray Absorption Spectra of $CeO_2$ and $CeFe_2$: New Examination by Using Resonant X-ray Emission Spectroscopy. *Mod. Phys. Lett. B* **2013**, *27* (16), 1330012.

(64) Sham, T. K.; Gordon, R. A.; Heald, S. M. Resonant Inelastic X-Ray Scattering at the Ce $L_3$ Edge of $CePO_4$ and $CeO_2$: Implications for the Valence of $CeO_2$ and Related Phenomena. *Phys. Rev. B: Condens. Matter Mater. Phys.* **2005**, *72* (3), 035113.

(65) Rice, N. T.; Popov, I. A.; Russo, D. R.; Gompa, T. P.; Ramanathan, A.; Bacsa, J.; Batista, E. R.; Yang, P.; La Pierre, H. S. Comparison of Tetravalent Cerium and Terbium Ions in a Conserved, Homoleptic Imidophosphorane Ligand Field. *Chem. Sci.* **2020**, *11* (24), 6149−6159.

(66) Sergentu, D.-C.; Autschbach, J. X-Ray Absorption Spectra of f-Element Complexes: Insight from Relativistic Multiconfigurational Wavefunction Theory. *Dalton Trans.* **2022**, *51* (5), 1754−1764.

(67) Sergentu, D.-C.; Duignan, T. J.; Autschbach, J. Ab Initio Study of Covalency in the Ground versus Core-Excited States and X-Ray Absorption Spectra of Actinide Complexes. *J. Phys. Chem. Lett.* **2018**, *9* (18), 5583−5591.

(68) Kaindl, G.; Kalkowski, G.; Brewer, W. D.; Perscheid, B.; Holtzberg, F. M-edge X-ray Absorption Spectroscopy of 4f Instabilities in Rare-earth Systems (Invited). *J. Appl. Phys.* **1984**, *55* (6), 1910−1915.

(69) Jo, T.; Kotani, A. Effect of Valence Mixing on Multiplet Structure in Core Photoabsorption Spectra for Ce Compounds. *Phys. Rev. B: Condens. Matter Mater. Phys.* **1988**, *38* (1), 830−833.

(70) Thole, B. T.; van der Laan, G.; Fuggle, J. C.; Sawatzky, G. A.; Karnatak, R. C.; Esteva, J.-M. 3d x-Ray-Absorption Lines and the $3d^94f^{n+1}$ Multiplets of the Lanthanides. *Phys. Rev. B: Condens. Matter Mater. Phys.* **1985**, *32* (8), 5107−5118.

(71) Hu, Z.; Kaindl, G.; Müller, B. G. Core-Level Spectroscopy of the Tetravalent Lanthanide Compounds $M_3LnF_7$ (with M = Cs, Rb; Ln = Ce, Pr, Nd, Tb, Dy). *J. Alloys Compd.* **1997**, *246* (1), 177−185.

(72) Kaindl, G.; Brewer, W. D.; Kalkowski, G.; Holtzberg, F. M-Edge X-Ray Absorption Spectroscopy: A New Tool for Dilute Mixed-Valent Materials. *Phys. Rev. Lett.* **1983**, *51* (22), 2056−2059.

(73) Kalkowski, G.; Kaindl, G.; Wortmann, G.; Lentz, D.; Krause, S. 4 f-Ligand Hybridization in $CeF_4$ and $TbF_4$ Probed by Core-Level Spectroscopies. *Phys. Rev. B: Condens. Matter Mater. Phys.* **1988**, *37* (3), 1376−1382.

(74) Manoubi, T.; Colliex, C.; Rez, P. Quantitative Electron Energy Loss Spectroscopy on $M_{45}$ Edges in Rare Earth Oxides. *J. Electron Spectrosc. Relat. Phenom.* **1990**, *50* (1), 1−18.

(75) Meihaus, K. R.; Minasian, S. G.; Lukens, W. W.; Kozimor, S. A.; Shuh, D. K.; Tyliszczak, T.; Long, J. R. Influence of Pyrazolate vs N-Heterocyclic Carbene Ligands on the Slow Magnetic Relaxation of Homoleptic Trischelate Lanthanide(III) and Uranium(III) Complexes. *J. Am. Chem. Soc.* **2014**, *136* (16), 6056−6068.

(76) de Groot, F.; Kotani, A. *Core Level Spectroscopy of Solids*, 1st ed.; CRC Press: Boca Raton, 2008.

(77) Moore, K. T.; van der Laan, G.; Haire, R. G.; Wall, M. A.; Schwartz, A. J. Oxidation and Aging in U and Pu Probed by Spin-Orbit Sum Rule Analysis: Indications for Covalent Metal-Oxide Bonds. *Phys. Rev. B: Condens. Matter Mater. Phys.* **2006**, *73* (3), 033109.

(78) Kotani, A.; Ogasawara, H. Theory of Core-Level Spectroscopy of Rare-Earth Oxides. *J. Electron Spectrosc. Relat. Phenom.* **1992**, *60* (4), 257−299.

(79) Stavitski, E.; de Groot, F. M. F. The CTM4XAS Program for EELS and XAS Spectral Shape Analysis of Transition Metal L Edges. *Micron* **2010**, *41* (7), 687−694.

(80) Minasian, S. G.; Keith, J. M.; Batista, E. R.; Boland, K. S.; Kozimor, S. A.; Martin, R. L.; Shuh, D. K.; Tyliszczak, T.; Vernon, L. J. Carbon K-Edge X-Ray Absorption Spectroscopy and Time-Dependent Density Functional Theory Examination of Metal−Carbon Bonding in Metallocene Dichlorides. *J. Am. Chem. Soc.* **2013**, *135* (39), 14731−14740.

(81) Minasian, S. G.; Keith, J. M.; Batista, E. R.; Boland, K. S.; Clark, D. L.; Conradson, S. D.; Kozimor, S. A.; Martin, R. L.; Schwarz, D. E.; Shuh, D. K.; Wagner, G. L.; Wilkerson, M. P.; Wolfsberg, L. E.; Yang, P. Determining Relative f and d Orbital Contributions to M−Cl Covalency in $MCl_6^{2-}$ (M = Ti, Zr, Hf, U) and $UOCl_5^-$ Using Cl K-Edge X-Ray Absorption Spectroscopy and Time-Dependent Density Functional Theory. *J. Am. Chem. Soc.* **2012**, *134* (12), 5586−5597.

(82) Minasian, S. G.; Keith, J. M.; Batista, E. R.; Boland, K. S.; Bradley, J. A.; Daly, S. R.; Kozimor, S. A.; Lukens, W. W.; Martin, R. L.; Nordlund, D.; Seidler, G. T.; Shuh, D. K.; Sokaras, D.; Tyliszczak, T.; Wagner, G. L.; Weng, T.-C.; Yang, P. Covalency in Metal−Oxygen Multiple Bonds Evaluated Using Oxygen K-Edge Spectroscopy and Electronic Structure Theory. *J. Am. Chem. Soc.* **2013**, *135* (5), 1864−1871.

(83) Branson, J. A.; Smith, P. W.; Arnold, J.; Minasian, S. G. Analyzing the Intensities of K-Edge Transitions in $X_2$ Molecules (X = F, Cl, Br) for Use in Ligand K-Edge XAS. *Inorg. Chem.* **2024**, *63* (34), 15557−15562.

(84) Su, J.; Batista, E. R.; Boland, K. S.; Bone, S. E.; Bradley, J. A.; Cary, S. K.; Clark, D. L.; Conradson, S. D.; Ditter, A. S.; Kaltsoyannis, N.; Keith, J. M.; Kerridge, A.; Kozimor, S. A.; Löble, M. W.; Martin, R. L.; Minasian, S. G.; Mocko, V.; La Pierre, H. S.; Seidler, G. T.; Shuh, D. K.; Wilkerson, M. P.; Wolfsberg, L. E.; Yang, P. Energy-Degeneracy-Driven Covalency in Actinide Bonding. *J. Am. Chem. Soc.* **2018**, *140* (51), 17977−17984.

(85) Wolfsberg, M.; Helmholz, L. The Spectra and Electronic Structure of the Tetrahedral Ions $MnO_4^-$, $CrO_4^{--}$, and $ClO_4^-$. *J. Chem. Phys.* **1952**, *20* (5), 837−843.

(86) Ionization Potentials of Atoms and Atomic Ions−Section 10. Atomic, Molecular, and Optical Physics. In *CRC Handbook of Chemistry and Physics*; Lide, D. R., Ed.; CRC Press, 2004; pp 10-178−10-180.

(87) Koopmans, T. Über die Zuordnung von Wellenfunktionen und Eigenwerten zu den Einzelnen Elektronen Eines Atoms. *Physica* **1934**, *1* (1−6), 104−113.

(88) Edelstein, N. M.; Lukens, W. W. F.-O. Mixing in the Octahedral $f^2$ Compounds $UX_6^{2-}$ [X = F, Br, Cl, I] and $PrCl_6^{3-}$. *J. Phys. Chem. A* **2020**, *124* (21), 4253−4262.

(89) Brewer, L. Energies of the Electronic Configurations of the Singly, Doubly, and Triply Ionized Lanthanides and Actinides. *J. Opt. Soc. Am.* **1971**, *61* (12), 1666−1682.

(90) Lukens, W. W.; Edelstein, N. M.; Magnani, N.; Hayton, T. W.; Fortier, S.; Seaman, L. A. Quantifying the $\sigma$ and $\pi$ Interactions between U(V) f Orbitals and Halide, Alkyl, Alkoxide, Amide and Ketimide Ligands. *J. Am. Chem. Soc.* **2013**, *135* (29), 10742−10754.

(91) Kutzelnigg, W. Chemical Bonding in Higher Main Group Elements. *Angew. Chem., Int. Ed.* **1984**, *23* (4), 272−295.

(92) Kaupp, M. The Role of Radial Nodes of Atomic Orbitals for Chemical Bonding and the Periodic Table. *J. Comput. Chem.* **2007**, *28* (1), 320−325.

(93) Pyykkö, P. Dirac-Fock One-Centre Calculations Part 8. The $^1\Sigma$ States of ScH, YH, LaH, AcH, TmH, LuH and LrH. *Phys. Scr.* **1979**, *20* (5−6), 647−651.

(94) Burns, G.; Axe, J. D. In *Optical Properties of Ions in Crystals*; Chrosswhite, H. M., Moos, H. W., Eds.; Interscience: New York, 1967.

(95) Whangbo, M.; Hoffmann, R. Counterintuitive Orbital Mixing. *J. Chem. Phys.* **1978**, *68* (12), 5498−5500.

(96) Pereiro, F. A.; Galley, S. S.; Jackson, J. A.; Shafer, J. C. Contemporary Assessment of Energy Degeneracy in Orbital Mixing with Tetravalent F-Block Compounds. *Inorg. Chem.* **2024**, *63* (21), 9687−9700.

(97) *CrysAlis PRO*; Agilent Technologies Ltd: Yarnton, Oxfordshire, England, 2013.

(98) Dolomanov, O. V.; Bourhis, L. J.; Gildea, R. J.; Howard, J. a. K.; Puschmann, H. OLEX2: A Complete Structure Solution, Refinement and Analysis Program. *J. Appl. Crystallogr.* **2009**, *42* (2), 339−341.

(99) Sheldrick, G. M. SHELXT − Integrated Space-Group and Crystal-Structure Determination. *Acta Crystallogr., Sect. A: Found. Adv.* **2015**, *71* (1), 3−8.

(100) Sheldrick, G. M. Crystal Structure Refinement with SHELXL. *Acta Crystallogr., Sect. C: Cryst. Struct. Commun.* **2015**, *71* (1), 3−8.

(101) George, G. N. *EDG_FIT*; Stanford Synchrotron Radiation Laboratory: Stanford Linear Accelerator Center: Stanford, CA, 2023.

(102) Booth, C. H.; Bridges, F. *Real-Space X-Ray Absorption Package (RSXAP)*; Wiley, 2021.

(103) Paparazzo, E.; Ingo, G. M.; Zacchetti, N. X-ray Induced Reduction Effects at $CeO_2$ Surfaces: An X-ray Photoelectron Spectroscopy Study. *J. Vac. Sci. Technol., A* **1991**, *9* (3), 1416−1420.

(104) Neese, F. Software Update: The ORCA Program System—Version 5.0. *Wiley Interdiscip. Rev.: Comput. Mol. Sci.* **2022**, *12* (5), No. e1606.

(105) Neese, F. The ORCA Program System. *Wiley Interdiscip. Rev.: Comput. Mol. Sci.* **2012**, *2* (1), 73−78.

(106) Stephens, P. J.; Devlin, F. J.; Chabalowski, C. F.; Frisch, M. J. Ab Initio Calculation of Vibrational Absorption and Circular Dichroism Spectra Using Density Functional Force Fields. *J. Phys. Chem.* **1994**, *98* (45), 11623−11627.

(107) Roos, B. O.; Lindh, R.; Malmqvist, P.-Å.; Veryazov, V.; Widmark, P.-O.; Borin, A. C. New Relativistic Atomic Natural Orbital Basis Sets for Lanthanide Atoms with Applications to the Ce Diatom and $LuF_3$. *J. Phys. Chem. A* **2008**, *112* (45), 11431−11435.

(108) Roos, B. O.; Lindh, R.; Malmqvist, P.-Å.; Veryazov, V.; Widmark, P.-O. Main Group Atoms and Dimers Studied with a New Relativistic ANO Basis Set. *J. Phys. Chem. A* **2004**, *108* (15), 2851−2858.

(109) Reiher, M. Douglas−Kroll−Hess Theory: A Relativistic Electrons-Only Theory for Chemistry. *Theor. Chem. Acc.* **2006**, *116* (1−3), 241−252.

(110) Raghavachari, K.; Trucks, G. W.; Pople, J. A.; Head-Gordon, M. A Fifth-Order Perturbation Comparison of Electron Correlation Theories. *Chem. Phys. Lett.* **1989**, *157* (6), 479−483.

(111) Riplinger, C.; Neese, F. An Efficient and near Linear Scaling Pair Natural Orbital Based Local Coupled Cluster Method. *J. Chem. Phys.* **2013**, *138* (3), 034106.

(112) Guo, Y.; Riplinger, C.; Becker, U.; Liakos, D. G.; Minenkov, Y.; Cavallo, L.; Neese, F. Communication: An Improved Linear Scaling Perturbative Triples Correction for the Domain Based Local Pair-Natural Orbital Based Singles and Doubles Coupled Cluster Method [DLPNO-CCSD(T)]. *J. Chem. Phys.* **2018**, *148* (1), 011101.

(113) Stoychev, G. L.; Auer, A. A.; Neese, F. Automatic Generation of Auxiliary Basis Sets. *J. Chem. Theory Comput.* **2017**, *13* (2), 554−562.

(114) Purvis, G. D.; Bartlett, R. J. A Full Coupled-cluster Singles and Doubles Model: The Inclusion of Disconnected Triples. *J. Chem. Phys.* **1982**, *76* (4), 1910−1918.

(115) Bozkaya, U.; Turney, J. M.; Yamaguchi, Y.; Schaefer, H. F.; Sherrill, C. D. Quadratically Convergent Algorithm for Orbital Optimization in the Orbital-Optimized Coupled-Cluster Doubles Method and in Orbital-Optimized Second-Order Møller-Plesset Perturbation Theory. *J. Chem. Phys.* **2011**, *135* (10), 104103.

(116) Glendening, E. D.; Landis, C. R.; Weinhold, F. NBO 6.0: Natural Bond Orbital Analysis Program. *J. Comput. Chem.* **2013**, *34* (16), 1429−1437.

(117) Li Manni, G.; Fdez Galván, I.; Alavi, A.; Aleotti, F.; Aquilante, F.; Autschbach, J.; Avagliano, D.; Baiardi, A.; Bao, J. J.; Battaglia, S.; Birnoschi, L.; Blanco-González, A.; Bokarev, S. I.; Broer, R.; Cacciari, R.; Calio, P. B.; Carlson, R. K.; Carvalho Couto, R.; Cerdán, L.; Chibotaru, L. F.; Chilton, N. F.; Church, J. R.; Conti, I.; Coriani, S.; Cuéllar-Zuquin, J.; Daoud, R. E.; Dattani, N.; Decleva, P.; de Graaf, C.; Delcey, M. G.; De Vico, L.; Dobrautz, W.; Dong, S. S.; Feng, R.; Ferré, N.; FilatovGulak, M.; Gagliardi, L.; Garavelli, M.; González, L.; Guan, Y.; Guo, M.; Hennefarth, M. R.; Hermes, M. R.; Hoyer, C. E.; Huix-Rotllant, M.; Jaiswal, V. K.; Kaiser, A.; Kaliakin, D. S.; Khamesian, M.; King, D. S.; Kochetov, V.; Krośnicki, M.; Kumaar, A. A.; Larsson, E. D.; Lehtola, S.; Lepetit, M. B.; Lischka, H.; López Ríos, P.; Lundberg, M.; Ma, D.; Mai, S.; Marquetand, P.; Merritt, I. C. D.; Montorsi, F.; Mörchen, M.; Nenov, A.; Nguyen, V. H. A.; Nishimoto, Y.; Oakley, M. S.; Olivucci, M.; Oppel, M.; Padula, D.; Pandharkar, R.; Phung, Q. M.; Plasser, F.; Raggi, G.; Rebolini, E.; Reiher, M.; Rivalta, I.; Roca-Sanjuán, D.; Romig, T.; Safari, A. A.; Sánchez-Mansilla, A.; Sand, A. M.; Schapiro, I.; Scott, T. R.; Segarra-Martí, J.; Segatta, F.; Sergentu, D. C.; Sharma, P.; Shepard, R.; Shu, Y.; Staab, J. K.; Straatsma, T. P.; Sørensen, L. K.; Tenorio, B. N. C.; Truhlar, D. G.; Ungur, L.; Vacher, M.; Veryazov, V.; Voß, T. A.; Weser, O.; Wu, D.; Yang, X.; Yarkony, D.; Zhou, C.; Zobel, J. P.; Lindh, R.; Lindh, R. The OpenMolcas Web: A Community-Driven Approach to Advancing Computational Chemistry. *J. Chem. Theory Comput.* **2023**, *19* (20), 6933−6991.

(118) Roos, B. O.; Taylor, P. R.; Sigbahn, P. E. M. A Complete Active Space SCF Method (CASSCF) Using a Density Matrix Formulated Super-CI Approach. *Chem. Phys.* **1980**, *48* (2), 157−173.

(119) Andersson, K.; Malmqvist, P.; Roos, B. O. Second-order Perturbation Theory with a Complete Active Space Self-consistent Field Reference Function. *J. Chem. Phys.* **1992**, *96* (2), 1218−1226.

(120) Malmqvist, P. Å.; Pierloot, K.; Shahi, A. R. M.; Cramer, C. J.; Gagliardi, L. The Restricted Active Space Followed by Second-Order Perturbation Theory Method: Theory and Application to the Study of $CuO_2$ and $Cu_2O_2$ Systems. *J. Chem. Phys.* **2008**, *128* (20), 204109.